Journal of Fluids and Structures 28 (2012) 434–455

Contents lists available at SciVerse ScienceDirect

Journal of Fluids and Structures

journal homepage: www.elsevier.com/locate/jfs

Fluid–structure interaction with pipe-wall viscoelasticity during water hammer

A. Keramat [a,b,*,1], A.S. Tijsseling [b,2], Q. Hou [b], A. Ahmadi [c,3]

[a] Department of Civil Engineering, Shahrood University of Technology, Iran
[b] Department of Mathematics and Computer Science, Eindhoven University of Technology, P.O. Box 513, 5600 MB Eindhoven, The Netherlands
[c] Department of Civil Engineering, Shahrood University of Technology, Post Code: 3619995161, Shahrood, Iran

ARTICLE INFO

Article history:
Received 1 March 2011
Accepted 2 November 2011
Available online 6 December 2011

Keywords:
Water hammer
Fluid transient
Pressure surge
Fluid–structure interaction
Pipe vibration
Plastic pipe
Viscoelasticity

ABSTRACT

Fluid–structure interaction (FSI) due to water hammer in a pipeline which has viscoelastic wall behaviour is studied. Appropriate governing equations are derived and numerically solved. In the numerical implementation of the hydraulic and structural equations, viscoelasticity is incorporated using the Kelvin–Voigt mechanical model. The equations are solved by two different approaches, namely the Method of Characteristics–Finite Element Method (MOC-FEM) and full MOC. In both approaches two important effects of FSI in fluid-filled pipes, namely Poisson and junction coupling, are taken into account. The study proposes a more comprehensive model for studying fluid transients in pipelines as compared to previous works, which take into account either FSI or viscoelasticity. To verify the proposed mathematical model and its numerical solutions, the following problems are investigated: axial vibration of a viscoelastic bar subjected to a step uniaxial loading, FSI in an elastic pipe, and hydraulic transients in a pressurised polyethylene pipe without FSI. The results of each case are checked with available exact and experimental results. Then, to study the simultaneous effects of FSI and viscoelasticity, which is the new element of the present research, one problem is solved by the two different numerical approaches. Both numerical methods give the same results, thus confirming the correctness of the solutions.

1. Introduction

There are four important items, which may affect classical water-hammer results: unsteady friction (UF), column separation (CS), fluid–structure interaction (FSI) and viscoelasticity (VE), each of which has been separately investigated and verified in various researches. With the inclusion of two or more of these items in the analysis, eleven possibilities are offered from which some combinations already have been studied and some have not. The combinations of VE and UF (Covas et al., 2004a,b, 2005; Duan et al., 2010; Soares et al., 2008), CS and UF (Bergant et al., 2008a,b; Bughazem and Anderson, 2000), FSI and UF (Elansary et al., 1994), FSI and CS (Fan and Tijsseling, 1992; Tijsseling and Vardy, 2005; Tijsseling et al., 1996) and VE and CS (Hadj-Taïeb and Hadj-Taïeb, 2009; Keramat et al., 2010; Soares et al., 2009) have

* Corresponding author at: Department of Civil Engineering, Shahrood University of Technology, Iran. Tel.: +989161117850.
E-mail addresses: alireza.keramat@gmail.com (A. Keramat), a.s.tijsseling@tue.nl (A.S. Tijsseling), q.hou@tue.nl (Q. Hou), a.ahmadi@shahroodut.ac.ir (A. Ahmadi).
[1] Visiting scholar at the Department of Mathematics and Computer Science, Eindhoven University of Technology.
[2] Tel.: +31 40 247 2755; fax: +31 40 244 2489.
[3] Tel./fax: +98 273 3300 259.

0889-9746/$ - see front matter © 2011 Elsevier Ltd. All rights reserved.
doi:10.1016/j.jfluidstructs.2011.11.001

Nomenclature

Scalars

A	cross-sectional area (m^2)
B	constants
c	wave speed (m/s)
D	inner diameter of pipe (m)
E	modulus of elasticity (Pa); spring "stiffness" in Kelvin–Voigt model (Pa)
e	pipe wall thickness (m)
F	force (N)
g	gravitational acceleration (m/s^2)
H	piezometric head (m)
I	convolution integral
J	creep compliance function of pipe wall material (Pa^{-1})
K	fluid bulk modulus (Pa)
L	pipe length (m); Laplace operator
l	element length, mesh spacing (m)
p, q	parameters in stress–strain relation
Q	discharge (m^3/s)
u	displacement (m)
V	cross-sectional averaged fluid velocity (m/s)
α_r	averaging factor for radial stress
α_v	opening ratio of valve
β	Newmark parameter
γ	constant
Δt	numerical time step, mesh spacing (s)
ε	strain $\partial u/\partial z$
θ	angle between the pipe axis and horizontal surface (rad)
λ	eigenvalue (m/s)
μ	viscosity of dashpot (kg/(m s))
ρ	mass density (kg/m^3)
σ	stress (Pa)
τ	retardation time (s)
υ	Poisson's ratio

Matrices and vectors

$\mathbf{A}$, $\mathbf{B}$	coefficient matrices of the four FSI equations
$\mathbf{f}$	element force vector (up to a constant factor)
$\mathbf{K}$ ($\mathbf{M}$)	stiffness (mass) matrix of each element (up to a constant factor)
$\mathbf{r}$	right-hand-side vector of the four FSI equations
$\mathbf{S}$, $\mathbf{T}$, $\mathbf{\Lambda}$	matrices used in the diagonalization of the four FSI equations
$\mathbf{s}$	vector of shape functions
$\mathbf{u}$	vector of axial displacements of each element

Subscripts and superscripts

0	steady state; leading spring in Kelvin–Voigt model
$\dot{}$ ($\ddot{}$)	first (second) derivative with respect to time
$'$	quasi-steady friction coefficient in Soares et al. (2008)
$''$	unsteady friction coefficient in Soares et al. (2008)
$'''$	viscoelasticity coefficient
$''''$	Poisson coupling coefficient
$\bar{}$	Laplace transformed variable
A_1, A_2, A_3, A_4	computational sections at previous time
D	dashpot
f	fluid
KV	Kelvin–Voigt
k	number of each Kelvin–Voigt element
n	negative characteristic line
P	unknown computational variable
p	positive characteristic line
r	radial direction
S	spring
t	pipe, tube
v	valve
z	axial direction of pipe
ϕ	circumferential direction of pipe

already been investigated. The remaining combination of two, namely FSI and VE, is the scope of this article. Combinations of three were modelled by Neuhaus and Dudlik (2006) (CS, UF and FSI) and Warda and Elashry (2010) (CS, UF and VE).

Fluid–structure interaction deals herein with the transfer of momentum and forces between a pipeline and its contained fluid. This matter has been investigated widely for elastic pipes and various experimental and numerical researches have been reported (Tijsseling, 1996; Wiggert and Tijsseling, 2001). In the numerical researches (most of which are in the time domain as opposed to the frequency domain), solutions based on the Method of Characteristics (MOC), the Finite Element Method (FEM), or a combination of these, are predominant. Lavooij and Tijsseling (1991) presented two different procedures for computing FSI effects: full MOC uses MOC for both hydraulic and structural equations and in MOC–FEM the hydraulic equations are solved by the MOC and the structural equations by the FEM. Using the MOC–FEM approach, Ahmadi and Keramat (2010) investigated various types of junction coupling. Heinsbroek (1997) compared MOC and FEM for solving the structural beam equations for the pipes and his conclusion for axial vibration was that both full MOC and MOC–FEM are valid methods that give equivalent results. In the current research, these two approaches were selected and developed for transients in pipes with viscoelastic walls.

For pipes made of plastic such as polyethylene (PE), polyvinyl chloride (PVC) and acrylonitrile butadiene styrene (ABS), viscoelasticity is a crucial mechanical property that changes the hydraulic and structural transient responses. Covas et al. (2004a, 2005) presented a model that deals with the dynamic effects of pipe-wall viscoelasticity for hydraulic transients. The model included an additional term in the continuity equation to describe the retarded radial wall deformation based on a creep function fitted to experimental data. The governing equations were solved using MOC and it was said that, unlike the classical water-hammer model, only a model that includes viscoelasticity can predict accurately transient pressures. A more detailed research in this field by Soares et al. (2008) gave a general algorithm to include viscoelasticity and unsteady friction within the conventional MOC solution procedure. Their final conclusion that unsteady friction effects are negligible when compared to

pipe-wall viscoelasticity was partially confirmed by Duan et al. (2010). Frequency-dependent pressure wave propagation in viscoelastic pipes was studied by Prek (2004, 2007) using wavelets and transfer functions, respectively.

Papers dealing with both viscoelasticity and fluid–structure interaction are relatively rare. Williams (1977) performed FSI experiments in a 12 m long ABS pipe (27 mm inner diameter, 3.2 mm wall thickness). He stated that ABS is not significantly viscoelastic, and therefore not the main mechanism for dispersion (degradation of wave front). A thorough theoretical analysis and illustration of the degradation of wave fronts, as caused by FSI and viscoelasticity, was given by Bahrar et al. (1998). Weijde (1985) did experiments on a 50 mm diameter PVC pipeline containing a 24 m long U-shaped test section. An adjustable spring was used to vary the stiffness of the system. Rachid and Stuckenbruck (1989) presented a model for FSI transients in plastic pipes assuming that the viscoelastic behaviour of the pipe walls is solely due to pure shear. They tested their model for straight and Z-shaped pipe systems and concluded that the high frequencies caused by FSI virtually vanished as a result of viscoelasticity by the end of the first water-hammer cycle. In later works the classical water-hammer equations were extended to include plastic circumferential (hoop) deformations, offering models for elasto-plastic (Rachid and Costa Mattos, 1995, 1998b) or elasto-viscoplastic (Rachid et al., 1994) pipe materials. These models were developed with the aim of estimating the damage accumulation and lifetime prediction of industrial pipe systems. In addition, the FSI research by Rachid and Costa Mattos (1998a) provided a formulation and corresponding numerical solution for assessing structural failure due to fluid transients. Tijsseling and Vardy (1996) studied the effects of suppression devices on water hammer and pipe vibration. It was demonstrated that a short plastic extension significantly influenced the axial vibration of a water-filled steel pipe. With longer plastic sections a significant reduction in the amplitude of vibration was predicted. In another experiment on the damping of water hammer due to viscoelastic effects, Tijsseling et al. (1999) investigated water hammer in a steel pipeline fitted with an internal air-filled plastic tube of rectangular cross-section. Hachem and Schleiss (2011) modelled viscoelasticity and FSI to determine wave speeds in steel-lined rock-bored tunnels. Most recently, Achouyab and Bahrar (2011) published a numerical study on water hammer with FSI and viscoelasticity – similar to ours – in which the MOC–FEM approach was used to solve the equations. All cited simulations of water hammer in viscoelastic pipes did not consider the issue of support and elbow motion, something that can hardly be avoided in practice (Hambric et al., 2010; Heinsbroek and Tijsseling, 1994; Tijsseling and Heinsbroek, 1999). The present research aims at providing a mathematical model and its numerical solution for the inclusion of this matter.

The contribution of the current research compared to previous studies on FSI or viscoelasticity in fluid-filled pipes is that by taking into account both effects simultaneously, more extensive governing equations for the hydraulics and the structure are obtained. In addition, appropriate numerical solutions for them are proposed and verified. Validation of the developed mathematical model and its numerical solutions is carried out from different angles: axial vibration of a viscoelastic bar (or empty pipe), where the numerical solutions are validated against the available analytical solution; FSI in an elastic pipe, where the results are checked against exact results; water hammer in a viscoelastic pipe, where the experimental results of two case studies are used; FSI in a viscoelastic pipe – the new element of this research – where two different numerical solutions are compared.

2. Mathematical model

2.1. Viscoelasticity

Viscoelasticity concerns a mechanical response involving aspects of both elastic solids and viscous fluids. The one-dimensional mechanical response of a linear elastic solid is often represented by the mechanical analogue of a spring governed by $F_S = k_S u$ in which F is the force, u is the displacement and subscript S stands for the spring. The one-dimensional mechanical response of a linear viscous fluid is often represented by the mechanical analogue of a viscous damper characterised by $F_D = k_D \dot{u}$, in which subscript D stands for dashpot and the overdot represents the derivative with respect to time. To describe a viscoelastic linear response, one possible choice is a model that consists of a spring and a damper in parallel. Then it is clear that $F = F_S + F_D$ so that $F = k_S u + k_D \dot{u}$. According to this relation the mechanical model depicted in Fig. 1(a) is defined by the constitutive relation between stress, σ, and strain, ε, as follows:

$$p_0\sigma = q_0\varepsilon + q_1\dot{\varepsilon}, \text{ with } p_0 = 1, \quad q_0 = E, \quad q_1 = \mu, \tag{1}$$

where E is the modulus of elasticity represented by the spring, μ is the viscosity represented by the dashpot and $\dot{\varepsilon}$ is the strain rate.

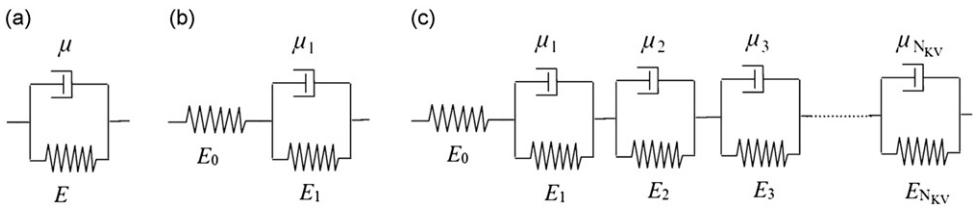

Fig. 1. Mechanical representation of a viscoelastic solid: (a) one Kelvin–Voigt element, (b) three-parameter Kelvin–Voigt model and (c) generalised Kelvin–Voigt model.

Fig. 1(a) depicts the Kelvin–Voigt model consisting of one element. It does not provide a satisfactory prediction of observed viscoelastic responses. The generalised Kelvin–Voigt model depicted in Fig. 1(c) is a more reliable representation. It consists of N_{KV} Kelvin–Voigt elements connected in series. By performing a similar analysis leading to Eq. (1) (see Appendix A for the three-parameter Kelvin–Voigt model depicted in Fig. 1(b)), one can prove that the constitutive equation for the generalised Kelvin–Voigt model has the form

$$p_0\sigma+\sum_{k=1}^{N_{KV}} p_k\frac{d^k\sigma}{dt^k}=q_0\varepsilon+\sum_{k=1}^{N_{KV}} q_k\frac{d^k\varepsilon}{dt^k}, \tag{2}$$

where the coefficients p and q are functions of modulus of elasticity and viscosity of each element, respectively, indicated by indices 1–N_{KV} (see Fig. 1(c)). So, the relation between stress and strain for linear viscoelastic materials involves higher-order time derivatives of both stress and strain. By applying the Laplace transform and its inverse to Eq. (2) (Wineman and Rajagopal, 2000) or using Boltzmann's superposition principle (Brinson and Brinson, 2008), an alternative way to represent strain in terms of stress is

$$\varepsilon(t)=\sigma(t)J(0)+\int_0^t \sigma(t-s)\frac{dJ}{ds}(s)ds=(\sigma*dJ)(t)=(J*d\sigma)(t), \tag{3}$$

in which "$*$" is the convolution operator and "$*d$" is the Stieltjes convolution operator (see Appendix A, Eq. (A.19)) which includes the term $\sigma(t)J(0)$ representing the immediate response. The creep compliance function $J(t)$ corresponding to the generalised Kelvin–Voigt model (Fig. 1(c)) is given by

$$J(t):=J_0+\sum_{k=1}^{N_{KV}} J_k(1-e^{-(t/\tau_k)}), \tag{4}$$

where $J_0=J(0):=1/E_0$ represents the immediate response of the material; J_k defined by $J_k:=1/E_k$ is the creep compliance of the spring of the kth Kelvin–Voigt element; E_k is the modulus of elasticity of the kth spring and τ_k is the retardation time of the kth dashpot. The time scale is $\tau_k:=\mu_k/E_k$ in which μ_k is the viscosity of the kth dashpot. Eqs. (2) and (3) are proved for the three-parameter Kelvin–Voigt solid depicted in Fig. 1(b), in Appendix A.

Relation (3) indicates that the total strain consists of an immediate part and a retarded part. The retarded part is a function of the whole history of loading in combination with the creep compliance. This is in fact the accumulated response to step loadings till the current time. In an FSI problem, the loading is related to the fluid and the structure. Fluid pressure within the pipe causes hoop stress and hoop strain which has an immediate and a retarded part. The pressure load is governed by the continuity and momentum equations for the fluid. If Poisson contraction is taken into account, then the hoop stress causes axial strain which again is composed of immediate and retarded parts. This is referred to as the Poisson coupling effect. Unbalanced fluid pressure can lead to moving valves and elbows, generating axial strains in the pipes (junction coupling).

The steady pressure head, H_0, fully determines the static response of the structure. As the dynamic response is of interest here, the dynamic head $\tilde{H}:=H-H_0$ is used in the coming formulations. In view of this and considering Eqs. (3) and (4), three terms making up the retarded contributions are defined. The first one denoted by $I_{\tilde{H}}$ gives the retarded hoop strain [up to a constant factor $\rho gD/(2e)$],

$$I_{\tilde{H}}:=\int_0^t \tilde{H}(t-s)\frac{dJ}{ds}(s)ds=\sum_{k=1}^{N_{KV}}\left(\frac{J_k}{\tau_k}\int_0^t \tilde{H}(t-s)e^{-(s/\tau_k)}ds\right):=\sum_{k=1}^{N_{KV}} I_{\tilde{H}k}. \tag{5}$$

The second one, I_{σ_z}, represents the retarded axial strain defined by

$$I_{\sigma_z}:=\int_0^t \sigma_z(t-s)\frac{dJ}{ds}(s)ds=\sum_{k=1}^{N_{KV}}\left(\frac{J_k}{\tau_k}\int_0^t \sigma_z(t-s)e^{-(s/\tau_k)}ds\right):=\sum_{k=1}^{N_{KV}} I_{\sigma_z k}, \tag{6}$$

where σ_z is the axial dynamic stress in the pipe wall (total axial stress is calculated by $\sigma_{z,\text{total}}=\sigma_z+\sigma_{z,0}$ where $\sigma_{z,0}$ is the axial static stress due to the steady pressure head H_0).

The third one, $I_{\ddot{u}_z}$, is calculated from the axial acceleration $\ddot{u}_z$ of the viscoelastic-pipe wall,

$$I_{\ddot{u}_z}:=\int_0^t \ddot{u}_z(t-s)\frac{dJ}{ds}(s)ds=\sum_{k=1}^{N_{KV}}\left(\frac{J_k}{\tau_k}\int_0^t \ddot{u}_z(t-s)e^{-(s/\tau_k)}ds\right):=\sum_{k=1}^{N_{KV}} I_{\ddot{u}_z k}. \tag{7}$$

This is proportional to the retarded axial stress gradient caused by inertia forces. Expressions (5)–(7) will be employed in the next section to conveniently formulate the governing equations.

Relation (3) holds for uniaxial loading and if one wants to extend it to three-directional loading, then deformations related to Poisson's ratio, υ (an important material property which in viscoelastic materials is a function of time), have to be taken into account. According to Stieltjes convolution notation (expression (A.19)) the three-directional constitutive relation between stress and strain in the z-direction of a r,ϕ,z cylindrical coordinate system reads (Wineman and Rajagopal, 2000)

$$\varepsilon_z=\sigma_z*dJ-(\varepsilon_\phi+\varepsilon_r)*d\upsilon=\sigma_z*dJ-(\sigma_\phi*dJ)*d\upsilon-(\sigma_r*dJ)*d\upsilon. \tag{8}$$

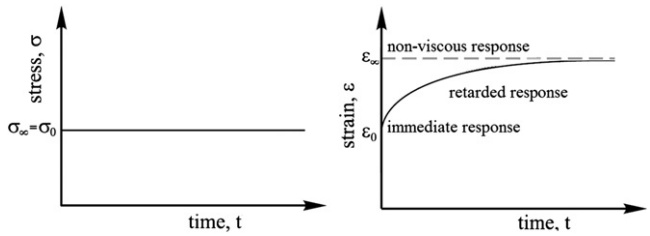

Fig. 2. Creep test on a viscoelastic bar.

Two simplifying assumptions are now made in Eq. (8). First, the Poisson ratio is assumed to be constant resulting in

$$\varepsilon_z = \sigma_z * dJ - \upsilon(\sigma_\phi * dJ - \sigma_r * dJ). \tag{9}$$

Secondly, considering the hoop and radial stress in thin-walled pipes,

$$\sigma_\phi = \frac{D}{2e}\rho_f g\tilde{H} \quad \text{and} \quad \sigma_r = -\alpha_r \rho_f g\tilde{H}, \tag{10}$$

where $\tilde{H}$ is the dynamic gauge pressure head and α_r is an averaging factor (1/2 according to Rachid and Stuckenbruck (1989) and 3/4 according to Tijsseling (2007)). Furthermore, σ_r is neglected compared to σ_ϕ, so that Eq. (9) becomes

$$\varepsilon_z = \sigma_z * dJ - \upsilon(\sigma_\phi * dJ). \tag{11}$$

This relation and a similar relation holding for the ϕ-direction are used in deriving the governing equations for viscoelastic FSI problems.

To clarify the nature of viscoelastic solids, the result of a creep test on a viscoelastic bar is shown in Fig. 2. In the creep test, a step uniaxial stress σ_0 is suddenly applied to the bar without causing inertia effects. For this case, $\varepsilon_0 := \sigma_0 J_0$ and according to Eqs. (3) and (4) one can write

$$\varepsilon = \sigma_0 * dJ = \sigma_0\left(J_0 + \sum_{k=1}^{N_{KV}} J_k(1-e^{-(t/\tau_k)})\right), \text{ so that } \varepsilon_\infty = \lim_{t\to\infty}\varepsilon = \sigma_0 J_0 + \sigma_0 \sum_{k=1}^{N_{KV}} J_k = \sigma_0 \sum_{k=0}^{N_{KV}} J_k. \tag{12}$$

This example illustrates how the strain responses in a viscoelastic bar and in an elastic bar differ when a constant stress is suddenly applied. The deformation mechanism associated with the creep is related to the long chain molecular structure of polymers. Continuous loading gradually induces strain accumulation in creep as the polymer molecules rotate and unwind to accommodate the load (Brinson and Brinson, 2008). The dynamic response (including inertia effects) to a suddenly applied step stress is elucidated in Section 4.1.1.

To find the actual creep behaviour of a viscoelastic material, there is no other way than performing experiments, because of its dependence on the molecular structure, the temperature and the loading history of the material. To characterize this behaviour, the creep compliance function, $J(t)$, given in Eq. (3), is usually used. There are two ways to determine this function which both rely on experimental data. In the first one, creep tests are done in the laboratory for one specific material and temperature with quasi-static or dynamic loading. However, this approach cannot accurately determine the creep function for practical situations, because it is very sensitive to the history of loading as well as the configuration of the test. The second way, which has been used by Covas et al. (2005), is by performing a calibration experiment in the field or in the test facility and then running a numerical solver to tune the unknown coefficients of the proposed mechanical model. The aim is to obtain appropriate coefficients such that the transient solver based on those coefficients gives numerical results as close as possible to those of the experiments. This so-called creep calibration allows for reliably doing all numerical simulations for one specific facility only. If these calibrated values are available and not affected by FSI itself, then an FSI analysis can be performed to obtain transient hydraulic and structural responses.

2.2. Governing equations for water hammer with FSI in a viscoelastic pipe

The equations for water hammer in an axially and radially vibrating pipe are derived. If the pipe wall is made of a viscoelastic material, then besides the immediate strain, there is also a retarded strain which responds gradually in time to internal or external loading. During a transient flow, this retarded deformation causes mechanical damping, influencing not only the fluid dynamics but also the structural response.

It is assumed that the piping system consists of thin-walled and linearly viscoelastic pipes for which the radial inertia and radial shear and bending deformation of walls are neglected. The other structural assumptions are that there is no buckling and no large deformations. Viscoelasticity is simulated by the Kelvin–Voigt model and only axial pipe vibration is considered.

For the hydraulic equations, the assumptions of no friction and no column separation are made. The frictionless system is a sensible assumption because in the numerical results confirmed by experiments (Covas et al., 2004b, 2005; Keramat et al., 2010) it is seen that in viscoelastic pipes the dynamic effect of viscoelasticity is significantly larger than that of friction. In addition, accurate UF-FSI models do not exist.

The following extended water-hammer equations for fluid velocity V and piezometric head H include FSI Poisson coupling. Viscoelastic effects of the pipe wall are taken into account by a retarded strain term in the continuity equation (see Appendix B):

$$\frac{\partial V}{\partial z}+\frac{g}{c_f^2}\frac{\partial H}{\partial t}-2\upsilon\frac{\partial \dot{u}_z}{\partial z}=\rho_f g(\upsilon^2-1)\frac{D}{e}\frac{\partial I_{\tilde{H}}}{\partial t}, \tag{13}$$

$$\frac{\partial V}{\partial t}+g\frac{\partial H}{\partial z}=0, \tag{14}$$

in which z is the axial coordinate, t is time, g is the gravitational acceleration, $\dot{u}_z$ is the axial pipe velocity, D is the inner pipe diameter, υ is Poisson's ratio, ρ_f is the fluid density, e is the wall thickness, $I_{\tilde{H}}$ is the retarded circumferential strain (up to a constant factor) given by relation (5) and c_f is the classical pressure wave speed defined by

$$c_f:=\left(\rho_f\left(\frac{1}{K}+(1-\upsilon^2)\frac{D}{eE_0}\right)\right)^{-(1/2)}, \tag{15}$$

where E_0 is Young's modulus of elasticity corresponding to the immediate hoop strain and K is the bulk modulus of the liquid. Poisson's ratio in viscoelastic materials is larger than in most elastic materials, so the Poisson coupling governed by the third term in Eq. (13) is more important in viscoelastic pipes, although the important ratio D/e is usually larger than in elastic pipes.

Previous models on water hammer in viscoelastic pipes (Covas et al., 2004a,b, 2005; Soares et al., 2008), only solve Eqs. (13) and (14) and neglect the Poisson coupling term in Eq. (13). So they assume $\dot{u}_z=0$ throughout the pipeline. This assumption is only valid if the entire pipeline is fully restrained from axial movements, which is a hard task in practice.

The second set of equations governs the axial vibration of the pipe wall. The first equation is obtained by taking the time derivative of Eq. (11) for a thin-walled pipe of constant Poisson's ratio and using the Stieltjes convolution operator given by Eq. (A.19) (The derivation is similar to that of Eq. (13) in Appendix B):

$$\frac{\partial \dot{u}_z}{\partial z}-\frac{1}{\rho_t c_t^2}\frac{\partial \sigma_z}{\partial t}+\rho_f g\frac{\upsilon D}{2eE_0}\frac{\partial H}{\partial t}=\frac{\partial I_{\sigma_z}}{\partial t}-\rho_f g\frac{\upsilon D}{2e}\frac{\partial I_{\tilde{H}}}{\partial t}, \quad \text{with} \tag{16}$$

$$c_t^2:=\frac{E_0}{\rho_t}, \tag{17}$$

where c_t is the classical wave speed in solid bars, ρ_t is the density of the pipe material, and $I_{\tilde{H}}$ and I_{σ_z} are given by relations (5) and (6), respectively. The second equation is conservation of momentum which herein does not include any friction, gravity and viscoelastic effects:

$$\frac{\partial \dot{u}_z}{\partial t}-\frac{1}{\rho_t}\frac{\partial \sigma_z}{\partial z}=0. \tag{18}$$

Eqs. (18) and (16) can be combined into one second-order partial differential equation for the axial pipe displacement u_z (see Appendix C):

$$\frac{\partial^2 u_z}{\partial t^2}-c_t^2\frac{\partial^2 u_z}{\partial z^2}-g\frac{\rho_f}{\rho_t}\frac{\upsilon D}{2e}\frac{\partial \tilde{H}}{\partial z}-E_0 g\frac{\rho_f}{\rho_t}\frac{\upsilon D}{2e}\frac{\partial I_{\tilde{H}}}{\partial z}+E_0 I_{\ddot{u}_z}=0, \tag{19}$$

where $I_{\ddot{u}_z}$ is given by relation (7). Eq. (19) governs the axial vibration of a pipe with viscoelastic wall interacting with an internal unsteady pressure. In this research, it is used in the MOC–FEM solution procedure.

2.3. Initial and boundary conditions

Appropriate initial conditions for the structural and hydraulic variables have to be included in the model to solve each problem. These are the static structural state in advance of the initiation of the transient event and the steady state flow in the hydraulic model.

Regarding the boundary conditions, for simulating Poisson and/or junction coupling, a specific relation should be used. Generally, junction coupling is the interaction between fluid and structure occurring at boundaries. For a simple reservoir-pipe-valve system, which is the case considered herein, a constant reservoir-head and zero-structural velocity hold at the upstream boundary, while for the free downstream valve of zero mass and with gradual closure the relations are

$$\frac{V-\dot{u}_z}{V_0}=\alpha_v\sqrt{\frac{\tilde{H}+H_0}{H_0}}, \tag{20}$$

$$\sigma_z A_t=\rho_f g\tilde{H}A_f, \quad \tilde{H}:=H-H_0, \tag{21}$$

where A_f and A_t are the cross-sectional areas of flow and tube wall, respectively, and the time-dependent quantity α_v defines the resistance of the valve. To obtain a situation with only Poisson coupling, the valve is fixed to eliminate junction coupling. Relation (21) is then replaced by

$$\dot{u}_z = 0. \tag{22}$$

3. Numerical solution

Two different numerical approaches are used to investigate FSI in pipes with viscoelastic walls: MOC–FEM and full MOC. The solution processes are similar to the cases of elastic pipes (Lavooij and Tijsseling, 1991) except for the calculation of terms which contain (retarded) strains. The advantage of the MOC–FEM approach is that it can relatively easily be used when other phenomena involved in the transient analysis of fluid and structure, such as unsteady friction, column separation, viscoelasticity and plasticity, and large deformations or buckling, are of interest and intended to be inserted in the model. In the MOC–FEM method, the hydraulic equations are solved separately from the structural equations, so that all existing knowledge on classical water-hammer and pipe vibrations can be used. The method's disadvantage is that it requires coupling iterations in each time step to arrive at converged values for the hydraulic and structural variables causing the solution to take more time compared to full MOC. Furthermore, standard FEM cannot accurately deal with travelling discontinuities, but this matter is of less importance in practical applications, because events like pump failure or gradual valve closure rarely cause instantaneous jumps in pressure and velocity.

3.1. Treatment of convolution-integral terms

In the Eqs. (13), (16) and (19) there are terms with the convolution integrals I. These are approximated by functions of the unknowns at the current and previous time steps. This is done with the aid of two relations. If $I_k(t) := J_k/\tau_k \int_0^t h(t-s)\mathrm{e}^{-s/\tau_k} ds$, where h is an arbitrary real function, then an excellent approximation for the current type of convolution integrals using a stable recursive relation is (see Appendix D):

$$I_k(t): \\ = \frac{J_k}{\tau_k}\int_0^t h(t-s)\mathrm{e}^{-s/\tau_k} ds \approx h(t)\left(J_k - \frac{J_k\tau_k}{\Delta t}(1-\mathrm{e}^{-\Delta t/\tau_k})\right) + h(t-\Delta t)\left(-J_k\mathrm{e}^{-\Delta t/\tau_k} + \frac{J_k\tau_k}{\Delta t}(1-\mathrm{e}^{-\Delta t/\tau_k})\right) + \mathrm{e}^{-\Delta t/\tau_k} I_k(t-\Delta t). \tag{23}$$

The time derivative of $I_k(t)$ is conveniently calculated by

$$\frac{dI_k}{dt}(t) = -\frac{I_k(t)}{\tau_k} + \frac{J_k}{\tau_k}h(t), \tag{24}$$

where $I_k(t)$ on the right-hand side is the approximation (23).

3.2. MOC–FEM approach

The MOC is used to solve the hydraulic equations (13) and (14), and the FEM is employed to solve the equation of axial pipe vibration (19). To have a methodical form for the MOC implementation of Eqs. (13) and (14), table 2 in the paper by Soares et al. (2008) has been extended herein in Table 1 (with the friction coefficients set to zero) to include the structural effects of Poisson coupling. Junction coupling is implemented through the boundary conditions and its inclusion in the analysis does not affect the governing differential equations. In the MOC solution of Eqs. (13) and (14), first, they are transformed to ordinary differential equations and then they are written in finite-difference form on two characteristic lines denoted by C^+ and C^-

$$\mathrm{C}^+ : Q_P = -C_{a+}H_P + C_p, \tag{25}$$

$$\mathrm{C}^- : Q_P = C_{a-}H_P + C_n. \tag{26}$$

Here $Q = A_f V$ is the flow rate, subscript P indicates unknown quantities, and C_p, C_n, C_{a+}, C_{a-} are constants determined by the quantities obtained in the previous time step:

$$C_p := \frac{Q_{A_1} + BH_{A_1} + C'_{p1} + C''_{p1} + C'''_{p1} + C''''_{p1}}{1 + C'_{p2} + C''_{p2}}, \quad \text{with} \quad B := \frac{gA_f}{c_f}, \tag{27}$$

$$C_n := \frac{Q_{A_2} + BH_{A_2} + C'_{n1} + C''_{n1} + C'''_{n1} + C''''_{n1}}{1 + C'_{n2} + C''_{n2}}, \tag{28}$$

$$C_{a+} := \frac{B + C'''_{p2}}{1 + C'_{p2} + C''_{p2}}, \tag{29}$$

Table 1
Coefficients used in Eqs. (27)–(30).

Quasi-steady friction [′]: $C'_{p1}=C'_{p2}=0,\quad C'_{n1}=C'_{n2}=0$
Unsteady friction [″]: $C''_{p1}=C''_{p2}=0,\quad C''_{n1}=C''_{n2}=0$
Rheological behaviour of pipe-wall [‴]
Linear elastic: $C'''_{p1}=C'''_{p2}=0,\quad C'''_{n1}=C'''_{n2}=0$
Linear viscoelastic: $C'''_{p1}=-C'''_{n1}=-a_0a_2,\quad C'''_{p2}=C'''_{n2}=a_0a_1,\quad a_0=\frac{D}{e}A_f\rho_f g(1-\upsilon^2)c_f\Delta t,$
$a_1=\sum_{k=1}^{N_{KV}}\frac{J_k}{\Delta t}(1-e^{-(\Delta t/\tau_k)}),\quad a_2=(H(t-\Delta t)-H_0)\sum_{k=1}^{N_{KV}}\left(\frac{J_k}{\tau_k}e^{-(\Delta t/\tau_k)}\right)-H(t-\Delta t)a_1-\sum_{k=1}^{N_{KV}}\frac{e^{-(\Delta t/\tau_k)}}{\tau_k}I_{\tilde{H}k}(t-\Delta t)$
Poisson coupling [⁗]
No Poisson coupling: $C''''_{p1}=C''''_{n1}=0$
With Poisson coupling: $C''''_{p1}=-C''''_{n1}=2\upsilon A_f c_f\Delta t\frac{\partial\dot{u}_z}{\partial z}$

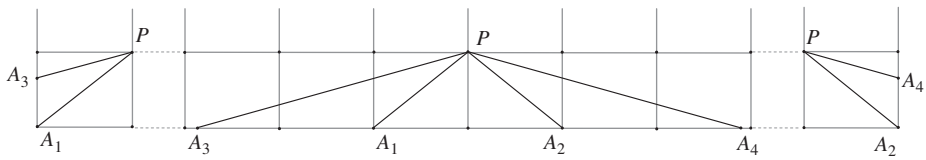

Fig. 3. Computational grid based on pressure waves and characteristic lines for interior nodes and nodes adjacent to boundaries.

$$C_{a-}:=\frac{B+C'''_{n2}}{1+C'_{n2}+C''_{n2}},\tag{30}$$

where the subscripts p and n stand for the "positive" and "negative" characteristic lines and unknowns holding the index A_1 (A_2) correspond to points on line C^+ (C^-) at the previous time step ($t-\Delta t$), see Fig. 3. Superscripts ′, ″, ‴ and ⁗ stand for quasi-steady friction, unsteady friction, pipe rheological behaviour and Poisson coupling, respectively. The finite-difference definition of each quantity is given in Table 1. The term on the right-hand-side of Eq. (13) is associated with viscoelasticity and is approximated using relations (23) and (24). To determine the term $\partial\dot{u}_z/\partial z$ in Eq. (13) and Table 1, the equation of axial vibration (19) has to be solved, but this in turn needs $\partial\tilde{H}/\partial z$ to be known from the hydraulic Eqs. (13) and (14). An iterative process between hydraulic and structural solvers leads to converged values for the unknowns at each time step (Heinsbroek, 1997; Lavooij and Tijsseling, 1991).

The FEM procedure for solving the structural Eq. (19) is similar to solving the axial vibration of a beam whose dynamic loading is axially distributed according to the hydraulic term $\partial\tilde{H}/\partial z$ (approximated by central finite difference). First the terms associated with viscoelasticity are approximated with the aid of formula (23) as follows:

$$\frac{\partial I_{\tilde{H}k}}{\partial z}(t)\approx\frac{\partial\tilde{H}}{\partial z}(t)\left(J_k-\frac{J_k\tau_k}{\Delta t}(1-e^{-\Delta t/\tau_k})\right)+\frac{\partial\tilde{H}}{\partial z}(t-\Delta t)\left(-J_ke^{-\Delta t/\tau_k}+\frac{J_k\tau_k}{\Delta t}(1-e^{-\Delta t/\tau_k})\right)+e^{-\Delta t/\tau_k}\frac{\partial I_{\tilde{H}k}}{\partial z}(t-\Delta t),\tag{31}$$

$$I_{\ddot{u}_zk}(t)\approx\ddot{u}_z(t)\left(J_k-\frac{J_k\tau_k}{\Delta t}(1-e^{-\Delta t/\tau_k})\right)+\ddot{u}_z(t-\Delta t)\left(-J_ke^{-\Delta t/\tau_k}+\frac{J_k\tau_k}{\Delta t}(1-e^{-\Delta t/\tau_k})\right)+e^{-\Delta t/\tau_k}I_{\ddot{u}_zk}(t-\Delta t).\tag{32}$$

Then, it is written in weak form and by application of Galerkin's method it reduces to the following system of equations for each finite element located between $z=z_a$ and $z=z_b$:

$$\rho_t(1+E_0b_1)\mathbf{M}\ddot{\mathbf{u}}+E_0\mathbf{K}\mathbf{u}=b_2\mathbf{f}+E_0\left[\mathbf{s}\frac{\partial u_z}{\partial z}\right]_{z_a}^{z_b},\tag{33}$$

where the quantities b_1 and b_2 are

$$b_1=\sum_{k=1}^{N_{KV}}\left(J_k-\frac{J_k\tau_k}{\Delta t}(1-e^{-\Delta t/\tau_k})\right),\tag{34}$$

$$b_2=g\rho_f\frac{\upsilon D}{2e}(1+E_0b_1)\frac{\partial\tilde{H}}{\partial z}(t)+g\rho_fE_0b_3\frac{\upsilon D}{2e}\frac{\partial\tilde{H}}{\partial z}(t-\Delta t)+g\rho_fE_0\frac{\upsilon D}{2e}\sum_{k=1}^{N_{KV}}\left(e^{-\Delta t/\tau_k}\frac{\partial I_{\tilde{H}k}}{\partial z}(t-\Delta t)\right)$$
$$-\rho_tE_0b_3\ddot{u}_z(t-\Delta t)+\rho_tE_0\sum_{k=1}^{N_{KV}}(e^{-\Delta t/\tau_k}I_{\ddot{u}_zk}(t-\Delta t))\text{ with}$$

$$b_3=\sum_{k=1}^{N_{KV}}\left(-J_ke^{-\Delta t/\tau_k}+\frac{J_k\tau_k}{\Delta t}(1-e^{-\Delta t/\tau_k})\right)\tag{35}$$

and $\mathbf{u}=\{u_{za}\ \ u_{zb}\}^{\mathrm{T}}$ and $\mathbf{s}$ are vectors of displacements and shape functions, respectively. If linear shape functions $\mathbf{s}=\{(z_b-z)/l\quad (z-z_a)/l\}^{\mathrm{T}}$ are used, then the matrices $\mathbf{M}$ and $\mathbf{K}$ and vector $\mathbf{f}$ become

$$\mathbf{M}=\frac{l}{6}\begin{bmatrix}2 & 1\\ 1 & 2\end{bmatrix},\quad \mathbf{K}=\frac{1}{l}\begin{bmatrix}1 & -1\\ -1 & 1\end{bmatrix},\quad \mathbf{f}=\frac{l}{2}\begin{Bmatrix}1\\ 1\end{Bmatrix}, \tag{36}$$

where $l=z_b-z_a$ is the length of the element. The last term of Eq. (33) will be explained in Section 3.4 in detail. To solve Eq. (33) in the time domain, the Newmark-β scheme with $\beta=1/4$ (constant average acceleration) was employed, because of its high accuracy and unconditional stability.

3.3. Full MOC approach

In this method, the four governing first-order partial differential Eqs. (14), (13), (18) and (16) are written in matrix form as

$$\mathbf{A}\frac{\partial \mathbf{y}}{\partial t}+\mathbf{B}\frac{\partial \mathbf{y}}{\partial z}=\mathbf{r}, \tag{37}$$

in which $\mathbf{y}$ and $\mathbf{r}$ are the vector of unknowns and the right-hand-side, respectively, and $\mathbf{A}$ and $\mathbf{B}$ are matrices of constant coefficients:

$$\mathbf{y}=\begin{Bmatrix}V\\ H\\ \dot{u}_z\\ \sigma_z\end{Bmatrix},\quad \mathbf{r}=\begin{Bmatrix}0\\ \rho_f g(\upsilon^2-1)\frac{D}{e}\frac{\partial I_{\tilde{H}}}{\partial t}\\ 0\\ \frac{\partial I_{\sigma_z}}{\partial t}-\rho_f g\frac{\upsilon D}{2e}\frac{\partial I_{\tilde{H}}}{\partial t}\end{Bmatrix},\quad \mathbf{A}=\begin{bmatrix}1 & 0 & 0 & 0\\ 0 & \frac{g}{c_f^2} & 0 & 0\\ 0 & 0 & 1 & 0\\ 0 & \rho_f g\frac{\upsilon D}{2eE_0} & 0 & \frac{-1}{\rho_t c_t^2}\end{bmatrix},\quad \mathbf{B}=\begin{bmatrix}0 & g & 0 & 0\\ 1 & 0 & -2\upsilon & 0\\ 0 & 0 & 0 & \frac{-1}{\rho_t}\\ 0 & 0 & 1 & 0\end{bmatrix}. \tag{38}$$

MOC transformation of these equations through a process described by Tijsseling (2003, 2009) and also discussed by Li et al. (2003), (see Appendix E herein), and then integration along the relevant characteristic lines connecting A_1 and A_2 with P corresponding to eigenvalues (wave speeds) $\hat{c}_f$ and $-\hat{c}_f$, and A_3 and A_4 to P corresponding to eigenvalues $\hat{c}_t$ and $-\hat{c}_t$ (see Fig. 3), yields the following compatibility equations

$$(\mathbf{TA})_{11}(V_P-V_{A_1})+(\mathbf{TA})_{12}(H_P-H_{A_1})+(\mathbf{TA})_{13}(\dot{u}_{zP}-\dot{u}_{zA_1})+(\mathbf{TA})_{14}(\sigma_{zP}-\sigma_{zA_1})=\Delta t[T_{11}r_1+T_{12}r_2+T_{13}r_3+T_{14}r_4], \tag{39}$$

$$(\mathbf{TA})_{21}(V_P-V_{A_2})-(\mathbf{TA})_{22}(H_P-H_{A_2})+(\mathbf{TA})_{23}(\dot{u}_{zP}-\dot{u}_{zA_2})-(\mathbf{TA})_{24}(\sigma_{zP}-\sigma_{zA_2})=\Delta t[T_{21}r_1+T_{22}r_2+T_{23}r_3+T_{24}r_4], \tag{40}$$

$$(\mathbf{TA})_{31}(V_P-V_{A_3})+(\mathbf{TA})_{32}(H_P-H_{A_3})+(\mathbf{TA})_{33}(\dot{u}_{zP}-\dot{u}_{zA_3})+(\mathbf{TA})_{34}(\sigma_{zP}-\sigma_{zA_3})=\Delta t[T_{31}r_1+T_{32}r_2+T_{33}r_3+T_{34}r_4], \tag{41}$$

$$(\mathbf{TA})_{41}(V_P-V_{A_4})-(\mathbf{TA})_{42}(H_P-H_{A_4})+(\mathbf{TA})_{43}(\dot{u}_{zP}-\dot{u}_{zA_4})-(\mathbf{TA})_{44}(\sigma_{zP}-\sigma_{zA_4})=\Delta t[T_{41}r_1+T_{42}r_2+T_{43}r_3+T_{44}r_4]. \tag{42}$$

Subscript P indicates the unknowns at the current time step and subscripts A_1, A_2, A_3 and A_4 indicate the calculated values at the previous time step, where each of the characteristic lines through P meets that earlier time line (Fig. 3). The slope of each characteristic line is equal to the reciprocal of the corresponding wave speed. Herein the numerical time step corresponds to the pressure wave grid ($\Delta t=\Delta z/\hat{c}_f$). The elements of matrix $\mathbf{T}$ in the Eqs. (39)–(42) are

$$\begin{aligned}
&T_{11}=T_{21}=1,\quad T_{12}=-T_{22}=\hat{c}_f,\quad T_{13}=T_{23}=2\upsilon\left(\frac{\hat{c}_f}{c_t}\right)^2\left(1-\left(\frac{\hat{c}_f}{c_t}\right)^2\right)^{-1},\\
&T_{14}=-T_{24}=2\upsilon\hat{c}_f\left(1-\left(\frac{\hat{c}_f}{c_t}\right)^2\right)^{-1},\quad T_{31}=T_{41}=\frac{-\rho_f\upsilon Dc_f^2}{2E_0e}\left(1-\left(\frac{c_f}{\hat{c}_t}\right)^2\right)^{-1},\\
&T_{32}=-T_{42}=\frac{-\rho_f\upsilon Dc_f^2\hat{c}_t}{2E_0e}\left(1-\left(\frac{c_f}{\hat{c}_t}\right)^2\right)^{-1},\quad T_{33}=T_{43}=1+\frac{2\rho_f\upsilon^2Dc_f^2}{2E_0e}\left(1-\left(\frac{c_f}{\hat{c}_t}\right)^2\right)^{-1},\\
&T_{34}=-T_{44}=\hat{c}_t.
\end{aligned} \tag{43}$$

The convolution integral terms in the vector $\mathbf{r}$ (Eq. (38)) are written in terms of the unknowns at the current and previous time steps using the relations (5), (6), (24) and approximation (23):

$$\frac{\partial I_{\tilde{H}k}(t)}{\partial t}\approx\tilde{H}(t)\left(\frac{J_k}{\Delta t}(1-e^{-\Delta t/\tau_k})\right)+\tilde{H}(t-\Delta t)\left(\frac{J_k}{\tau_k}\mathrm{e}^{-\Delta t/\tau_k}-\frac{J_k}{\Delta t}(1-e^{-\Delta t/\tau_k})\right)-\frac{\mathrm{e}^{-\Delta t/\tau_k}}{\tau_k}I_{\tilde{H}k}(t-\Delta t), \tag{44}$$

$$\frac{\partial I_{\sigma_zk}(t)}{\partial t}\approx\sigma_z(t)\left(\frac{J_k}{\Delta t}(1-\mathrm{e}^{-\Delta t/\tau_k})\right)+\sigma_z(t-\Delta t)\left(\frac{J_k}{\tau_k}\mathrm{e}^{-\Delta t/\tau_k}-\frac{J_k}{\Delta t}(1-\mathrm{e}^{-\Delta t/\tau_k})\right)-\frac{\mathrm{e}^{-\Delta t/\tau_k}}{\tau_k}I_{\sigma_zk}(t-\Delta t), \tag{45}$$

where time t corresponds to point P in Fig. 3.

Simultaneous solution of the compatibility Eqs. (39)–(42) in combination with the boundary conditions is performed at each time step with a constant inverse solution matrix. As the used grid is based on the pressure waves, characteristic lines corresponding to the stress waves do not necessarily meet the grid points at the previous time step (such as points A_3 and A_4

in Fig. 3). The remedy to this problem is linear interpolation using the known values at the nearest computational sections on the same time line. For points with characteristic lines that do not meet the previous time line (like points A_3 and A_4 at the boundaries), interpolation is done using the boundary values at the current and previous time step. In this case, it is necessary to first calculate the solution in the boundary nodes and then in the interior ones as the values on the boundaries of the current time step are required to perform the interpolation.

3.4. Implementation of the boundary conditions

In the MOC–FEM solution, boundary condition (20) defines the valve closure in the hydraulic equations and boundary condition (21) determines the applied hydraulic force in the structural equations if the valve is free to move. Eq. (33) is valid for interior and boundary elements. The global mass and stiffness matrices and the force vector of the entire system are formed in an assembly process. For the force vector in this process, the last term in Eq. (33) cancels for the interior nodes of a straight pipe and it becomes zero for the reservoir node.

For the valve node, the following expression, which is determined from the Eqs. (11), (21), (10) and (5), remains

$$\left.\frac{\partial u_z}{\partial z}\right|_{z_b=L} = [\sigma_z * dJ - \upsilon(\sigma_\phi * dJ)]_{z=L} = \rho_f g\left[\left(\frac{A_f}{A_t}\tilde{H}_P * dJ\right) - \frac{\upsilon D}{2e}(\tilde{H}_P * dJ)\right]$$
$$= \rho_f g\left(\frac{A_f}{A_t} - \frac{\upsilon D}{2e}\right)(\tilde{H}_P * dJ) = \rho_f g\frac{D}{2e}\left(\frac{1}{2}-\upsilon\right)\left(\frac{\tilde{H}_P}{E_0} + I_{\tilde{H}_P}\right), \quad \text{with} \quad \tilde{H}_P = H_P - H_{P,0}, \tag{46}$$

where L is the total length of the pipe and $I_{\tilde{H}_P}$ given by relation (5) is approximated by formula (23). Relation (46) is boundary condition (21) in terms of displacement as used in the last term of Eq. (33). It defines part of the hydraulic load on the free valve in the global force vector. It shows that for analysis including both coupling mechanisms, Poisson coupling terms – those with factor υ in Eq. (46) – contribute to the element-force vector (Eqs. (33)–(36)), in particular at the valve.

The valve boundary in the full MOC solution requires simultaneous solution of the compatibility Eqs. (39) and (41), associated with points A_1 and A_3, together with the coupling conditions (20) and (21). This has been done symbolically.

4. Numerical results

To validate the developed computer codes, several test problems are calculated and discussed in Section 4.1. To investigate the effects of simultaneous FSI and viscoelasticity, an actual pipeline was analysed for various situations in Section 4.2.

4.1. Validation

Three test problems are solved in this section, each of which is a special case of the general case of water hammer in a viscoelastic pipe experiencing FSI. The numerical results are verified against available semi-analytical solutions (Section 4.1.1), exact solutions (Section 4.1.2) and experiments (Section 4.1.3).

4.1.1. Vibration of a viscoelastic bar

Consider uniaxial wave propagation in a viscoelastic bar of length L, fixed at one end ($z=0$) and subjected to a suddenly applied constant axial force F_0 at the other end ($z=L$). The correspondence principle (see Appendix F) is used. This means that first the elastic response is obtained, after which $J_0=1/E_0$ in the elastic solution is replaced by $\bar{J}^*(s)=s\bar{J}(s)$ to arrive at the solution for the viscoelastic bar in the Laplace domain. Finally the desired response, i.e. the displacement field, is obtained in the time domain by numerically inverting $\bar{u}_z(z,s)$ from the Laplace to the time domain.

According to Eq. (19), by disregarding the terms associated with the internal pressure and viscoelasticity, the equation of motion for an elastic bar is

$$\frac{\partial^2 u_z}{\partial t^2} - c_t^2\frac{\partial^2 u_z}{\partial z^2} = 0. \tag{47}$$

The initial conditions are

$$u_z(z,0) = 0, \quad \frac{\partial u_z}{\partial t}(z,0) = 0, \tag{48}$$

and the boundary conditions are

$$u_z(0,t) = 0, \quad E_0\frac{\partial u_z}{\partial z}(L,t) = \frac{F_0}{A_t}. \tag{49a, b}$$

An exact solution based on Fourier series for the problem presented by Eqs. (47)–(49a, b) reads (see Appendix G)

$$u_z(z,t) = \frac{8}{\pi^2}\frac{F_0 L}{A_t E_0}\sum_{n=1,3,\ldots}^{\infty}\frac{(-1)^{(n-1)/2}}{n^2}\sin\frac{n\pi z}{2L}\left(1-\cos\frac{n\pi c_t t}{2L}\right). \tag{50}$$

Considering the creep compliance function $J(t)$ given by Eq. (4), the corresponding creep compliance $\bar{J}(s)$ in the Laplace domain is (see Appendix A for $N_{KV}=1$)

$$\bar{J}^*(s) := s\bar{J}(s) = s\left(\frac{1}{s}\sum_{k=0}^{N_{KV}} J_k - \sum_{k=1}^{N_{KV}} \frac{J_k\tau_k}{s\tau_k+1}\right) = J_0 + \sum_{k=1}^{N_{KV}} \frac{J_k}{s\tau_k+1}. \tag{51}$$

The viscoelastic response in the Laplace domain is obtained by taking the Laplace transform of Eq. (50) and replacing $J_0=1/E_0$ by $\bar{J}^*(s)$:

$$\bar{u}_z(z,s) = \frac{8}{\pi^2}\frac{F_0 L}{A_t}\bar{J}^*(s)\sum_{n=1,3,\ldots}^{\infty}\frac{(-1)^{(n+1)/2}}{n^2}\left(\sin\frac{n\pi z}{2L}\right)\left(\frac{s}{s^2+a(s)^2}-\frac{1}{s}\right), \quad \text{with} \quad a(s) = \frac{n\pi}{2L\sqrt{\rho_t\bar{J}^*(s)}}. \tag{52}$$

The algorithm of de Hoog et al. (1982) provided in a MATLAB code by Hollenbeck (Danish TU) was used for the numerical inversion of the Laplace transform. This algorithm works with complex values of s. Algorithms working with real values of s are simpler, but they give accurate results only for quasi-static cases and fail completely for the dynamic case (Narayanan and Beskos, 1982) and (Papargyri-Beskou and Beskos, 2004).

The results obtained with the (inverse) Laplace transform are used to validate the proposed FEM method for the structural equations as developed in Section 3.2. Eq. (33) is used without the terms containing internal pressure effects. Considering Eq. (3) and $\sigma_z(L,t)=F_0/A_t$, the boundary condition included in the last term of Eq. (33) (after assembling all elements) is treated as

$$\left.\frac{\partial u_z}{\partial z}\right|_{z=L} = [\sigma_z * dJ]_{z=L} = \left(\frac{F_0}{A_t} * dJ\right) = \frac{F_0}{A_t}J(t), \tag{53}$$

with $J(t)$ given by Eq. (4). This is similar to the boundary condition (49b), but now for the case that the bar is viscoelastic. For an elastic bar ($N_{KV}=0$), relation (53) reduces exactly to (49b).

The results for the test problem with the arbitrary specifications given in Table 2 for viscoelastic material no. 1 are shown in Fig. 4. It compares the transient responses of an elastic and a viscoelastic bar for the two applied solution methods (semi-analytical and FEM) for a time duration of 0.04 s. Results for the semi-analytical solution are displayed with 0.0005 s intentional shift to the right to ease comparison. There is good agreement between the two different solutions considering that each method involves different kinds of approximations: the semi-analytical solution has an approximation in the number of terms (waves) used to calculate the Fourier series (100 herein) and in the numerical implementation of the inverse Laplace transform, while the FEM has approximations associated with the time and space

Table 2
Specifications of a viscoelastic bar subjected to a uniaxial step load.

					Creep coefficients	k	1	2	3	4	5
F_0 (N)	ρ_t (kg/m^3)	$E_0=1/J_0$ (GPa)	A_t (m^2)	L (m)	Material no. 1	τ_k (s)	0.1	0.1	0.1	0.1	0.1
						J_k (10^{-10} Pa^{-1})	5	5	5	5	5
10	1000	2	0.01	4	Material no. 2	τ_k (s)	0.2	0.4	0.6	0.8	1
						J_k (10^{-10} Pa^{-1})	12	9	7	4	2

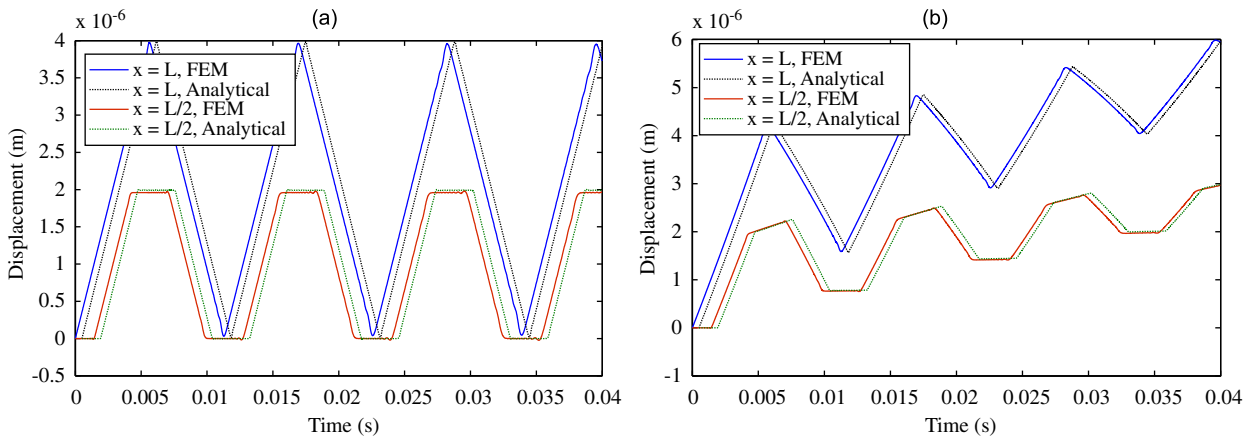

Fig. 4. Displacement at the end and the middle of a bar subjected to an axial step force for FEM solution (continuous lines) and analytical solution (broken lines). (a) Elastic bar and (b) viscoelastic bar.

discretizations as well as the numerical calculation of the convolution integrals dealing with viscoelasticity. Fig. 5 shows the response of the two materials for a duration of 10 times that in Fig. 4 to see how the oscillations damp out and the limit values are approached.

To obtain the static response (or dynamic response after a long time), considering Eq. (12) which gives the strain limit when time approaches infinity, one can calculate the limit for the displacement from $\varepsilon_z = \partial u_z/\partial z$ as

$$u_z = \frac{F_0}{A_t} z \sum_{k=0}^{N_{KV}} J_k. \tag{54}$$

This is Eq. (G.3) for $N_{KV}=0$. Even in elastic problems, the dynamic response after a long time converges to the static response if structural damping is taken into account; otherwise, the structure will oscillate forever around the static equilibrium position. The latter is the case in Fig. 4(a) where the static response at $x=L$ is calculated as 2×10^{-6} m. The period of oscillation of the elastic bar ($4L/c_t$) represents the time that the wave returns twice to the excitation point and is computed as 0.0114 s (Fig. 4(a)). This is much less than the retardation times indicating that the viscoelastic bar will fully creep after many oscillations (Fig. 5).

4.1.2. FSI in an elastic pipe

The Delft Hydraulics Benchmark Problem A consisting of a reservoir, a straight pipe and a valve with the specifications given in Table 3 is solved using the full MOC computer code (developed by the first author) to check the results against the exact results given by Tijsseling (2003). To verify the FSI code including Poisson and junction coupling, the massless valve is considered to be free to move and instantaneously closed. In Figs. 6 and 7 the obtained results for dynamic pressure at the valve and midpoint are successfully verified against the exact results.

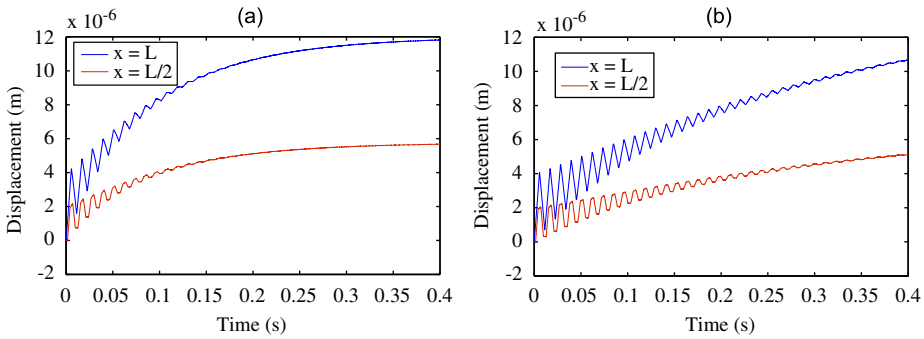

Fig. 5. Displacement at the end and the middle of a viscoelastic bar subjected to an axial step force for two different materials with the specifications given in Table 2. (a) Material no. 1 and (b) material no. 2.

Table 3
The properties of the pipeline according to the case study in (Tijsseling, 2003).

Length	Diameter	Thickness	Pipe's density	Young's modulus	Poisson's ratio	Pressure wave speed	Stress wave speed	Steady state velocity	Reservoir head
20 m	797 mm	8 mm	7900 kg/m^3	210 GPa	0.3	1024.7 m/s	5280.5 m/s	1 m/s	0 m

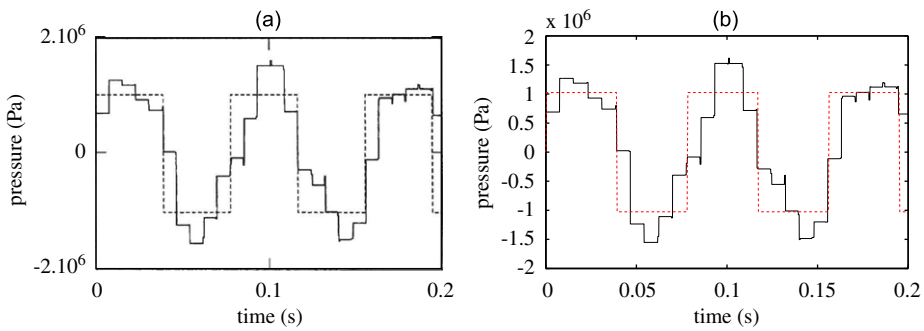

Fig. 6. Dynamic pressure at the valve for the Delft Hydraulics Benchmark Problem A. (a) Using the exact solution (Tijsseling, 2003) and (b) using the current numerical solution (full MOC). Broken lines show the classical water-hammer results.

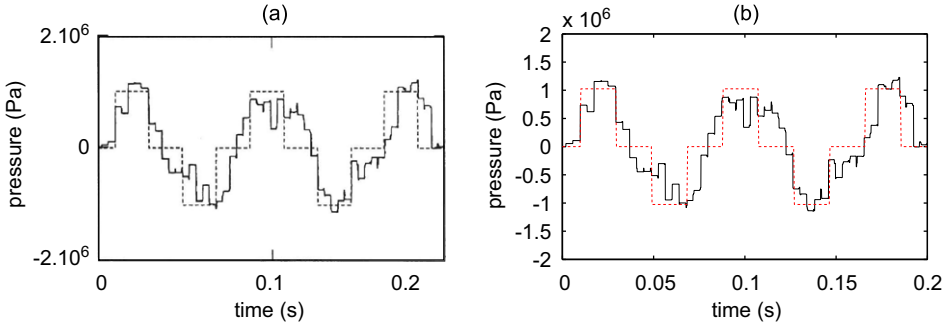

Fig. 7. Dynamic pressure at the midpoint for the Delft Hydraulics Benchmark Problem A. (a) Using the exact solution (Tijsseling, 2003) and (b) using the current numerical solution (full MOC). Broken lines show the classical water-hammer results.

Table 4
Specifications of the PVC pipe system at Deltares, Delft, The Netherlands, used to perform the water-hammer experiments.

PVC pipe length	Diameter of PVC pipe	Length of upstream steel pipe	Length of downstream steel pipe	Diameter of steel pipes	Young's modulus (PVC)	Young's modulus (steel)	Wave speed (PVC)	Wave speed (steel)
275.2 m	236 mm	20.6 m	13.8 m	200 mm	2.9 GPa	210 GPa	348 m/s	1200 m/s

Wall thickness of PVC pipe	Wall thickness of steel pipe	Friction coefficient	Time of valve closure	Steady state flow rate	Time step for simulation	Length of PVC pipe elements	Length of steel pipe elements
7.3 mm	3 mm	0.015	0.2 s	7 l/s	0.01 s	3.48 m	12 m

Table 5
Calibrated coefficients of the creep function for the Delft experiment with the specifications given in Table 4.

Sample size	Number of K-V elements	Retardation times		Creep compliance coefficients ($\times 10^{-10}$ Pa^{-1})	
50 s	2	$\tau_1=0.05$ s	$\tau_2=0.5$ s	$J_1=0.0924$	$J_2=0.1873$

4.1.3. Water hammer in a viscoelastic pipe

Tests have been conducted in a reservoir–pipeline–valve system consisting of a main viscoelastic (PVC) pipeline and two short iron pipes placed upstream and downstream of the main pipe. Rapid closure of a manually operated valve at the downstream end generated water hammer. The configuration of the system was discussed in detail by Laanearu et al. (2009) and Bergant et al. (2010). The results of this experiment and corresponding numerical simulations can be found in Bergant et al. (2011).

Before doing the numerical simulations, the hydraulic transient solver was calibrated (see Section 2.1). First the wave speed was estimated from the Joukowsky pressure rise ($\rho_f c_f V_0$) and then $J_0=1/E_0$ was determined from Eq. (15). The remaining $2N_{KV}$ parameters in the creep compliance function were obtained for varying N_{KV}. This calibration is a replacement for separate and independent creep tests. The unidentified parameters N_{KV}, τ_k and J_k ($k \geq 1$) of the viscoelastic model were estimated by inverse transient calculations in combination with an optimisation algorithm that minimises the difference between the measured and calculated heads at one selected pressure transducer (located at the valve herein). The MATLAB function "lsqnonlin", which solves nonlinear least-squares problems, was used for this purpose. Eventually, using the calibrated quantities in the transient solver, simulations with viscoelasticity were carried out to predict pressures at locations other than the selected one. The data used in the numerical simulation are specified in Table 4. The calibrated creep function coefficients appropriate for this experiment are given in Table 5.

Results of full MOC numerical simulations without FSI are compared against those of the physical experiment. This comparison is provided for the pressure history at the valve in Fig. 8(a) and at point P5, located 146.13 m downstream of the reservoir, in Fig. 8(b). Red and black lines correspond to the experimental and calculated results, respectively. The overall agreement between the experimental and numerical results is good. This verifies the implemented mathematical and numerical model for water hammer in viscoelastic pipes. The reason for the discrepancies is fully discussed by Bergant et al. (2011).

4.2. Case studies

An experiment performed at the Department of Civil and Environmental Engineering, Imperial College, London, with the specifications given in Table 6, is selected to define three case studies to be solved with the developed transient solvers.

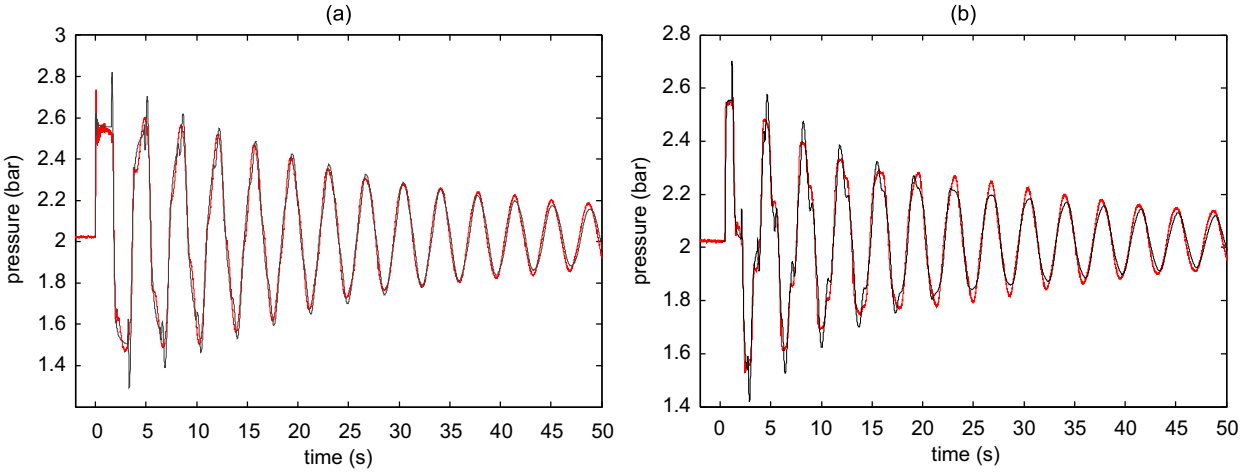

Fig. 8. Comparison of experimental (red) and numerical (black) pressures. (a) At the valve, and (b) at location P5. Viscoelasticity is taken into account, but FSI is not. (For interpretation of the references to color in this figure legend, the reader is referred to the web version of this article.)

Table 6
Specification of the reservoir–pipeline–valve experiment performed by Covas et al. (2004b, 2005).

Length	Inner diameter	Wall thickness	Young's modulus	Poisson's ratio	Steady state discharge	Reservoir head	Valve closure time	Pressure wave speed	Stress wave speed
277 m	50.6 mm	6.3 mm	1.43 GPa	0.46	1.01 l/s	45 m	0.09 s	360.2 m/s	630.0 m/s

Table 7
Calibrated creep coefficients J_k for the Imperial College test with $Q_0=1.01$ l/s and $c_f=395$ m/s, neglecting unsteady friction (Covas et al., 2005).

Sample size	Number of K–V elements	Retardation times τ_k (s) and creep coefficients J_k (10^{-10} Pa^{-1})				
20 s	5	$\tau_1=0.05$ $J_1=1.057$	$\tau_2=0.5$ $J_2=1.054$	$\tau_3=1.5$ $J_3=0.9051$	$\tau_4=5$ $J_4=0.2617$	$\tau_5=10$ $J_5=0.7456$

It is a reservoir–pipeline–valve system where the length between the vessel and the downstream globe valve is 277 m. In Section 4.2.1 this experiment is simulated for viscoelastic pipes without the effects of FSI. After arriving at exactly the same results as those of Covas et al. (2005), the pipes are assumed to be elastic but subjected to FSI effects in Section 4.2.2. In the last case study in Section 4.2.3, both FSI and viscoelasticity for the pipe system are taken into account. For cases including FSI, two different numerical solution methods were employed to predict the hydraulic and structural responses. For the FSI cases, the pipeline was considered to be straight and axially free to move to enhance Poisson coupling effects. The valve was allowed to displace to include junction coupling effects as well.

As mentioned in Section 2.1, viscoelastic behaviour is very sensitive with respect to certain properties such as non-homogeneity of the material, temperature and axial and circumferential pipe constraints. To have a reliable solver, the creep compliance function has to be calibrated for each pipe in the system. As, to the authors' knowledge, there is no explicit experimental data available including viscoelasticity and FSI simultaneously, accurate calibration of the creep function (using the proposed model) is impossible. To overcome this difficulty and have the necessary input for performing the numerical analysis, the creep function provided by Covas et al. (2004b, 2005) is used (Table 7). This function corresponds to high density polyethylene (HDPE) which is more viscous than PVC, so that larger retardation times and more Kelvin–Voigt elements are needed for an accurate description.

4.2.1. Viscoelasticity without FSI

In the Imperial College test, pipe sections were "rigidly" fixed to a wall and assumed to be constrained from any axial movement, so that there were no significant FSI effects in the experimental results. The MOC numerical results (including standard quasi-steady friction) for the heads at locations 1, 5 and 8 corresponding to distances from the upstream end of 271 m, 197 m and 116.5 m, respectively, are compared with the numerical and experimental results of Covas et al. (2005) in Fig. 9. The figure shows that viscoelasticity has been modelled and implemented herein correctly.

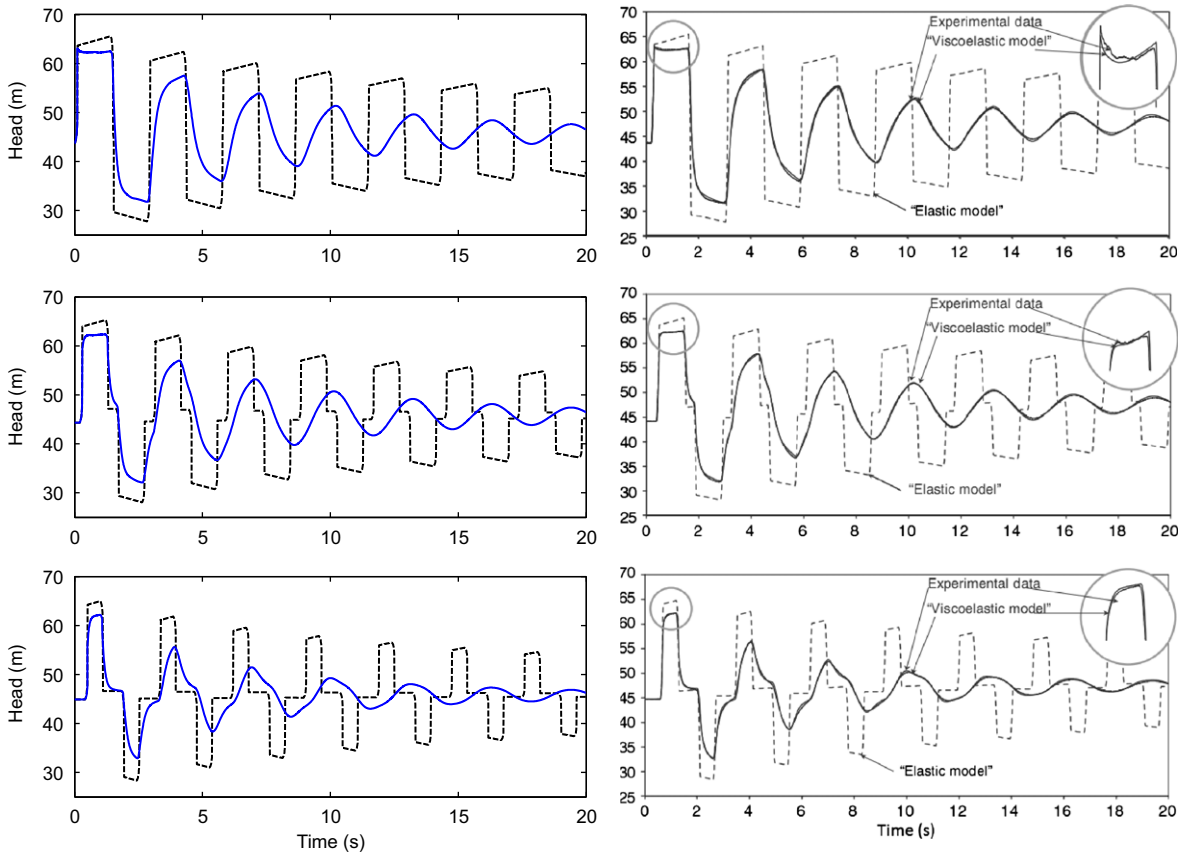

Fig. 9. Comparison of pressure heads calculated with viscoelasticity, but without FSI, for three locations; left: current model and right: Covas et al. (2005).

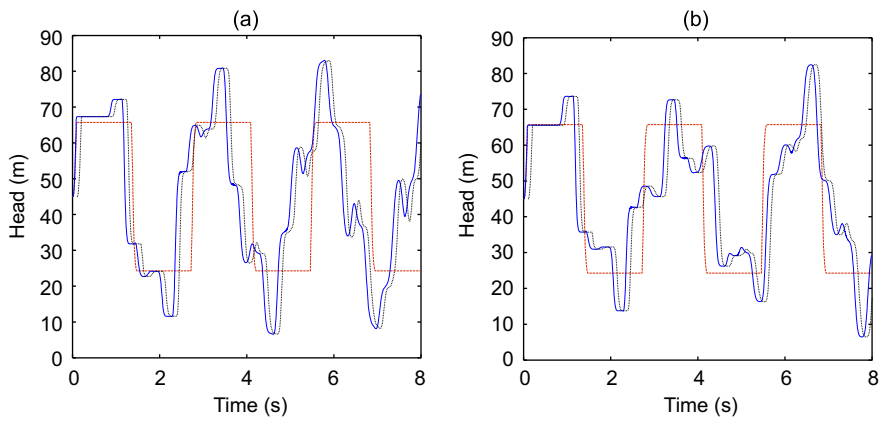

Fig. 10. Pressure head at the valve for the elastic model. (a) With only Poisson coupling, and (b) with Poisson and junction coupling. MOC–FEM solution in continuous blue lines and full MOC solution (with $t=0.1$ s intentional shift) in broken lines; dashed red lines correspond to classical water-hammer results. (For interpretation of the references to color in this figure legend, the reader is referred to the web version of this article.)

4.2.2. FSI without viscoelasticity

Now it is assumed that the pipeline is made from an elastic material and that there is no axial support throughout the pipeline thus allowing for significant Poisson coupling. If in addition the valve is free to move, junction coupling takes place too. Fig. 10 shows the results at location 1 (valve) for Poisson coupling only, and for Poisson and junction coupling together, using the two different numerical approaches. Broken black lines are the results of the full MOC solution, which are deliberately shifted to the right by 0.1 s to show any differences, and continuous blue lines are those of the MOC–FEM

solution. Dashed red lines depict the results of classical water-hammer. There is good agreement between each set of the results confirming the correct FSI implementation of both methods.

To obtain the classical water-hammer results, Poisson's ratio is set to zero so that the corresponding wave speed becomes 405 m/s (Eq. (15)), where it is 451.3 m/s if Poisson's ratio is 0.46. As a result, the wave speed and the Joukowsky pressure ($\rho_f c_f V_0$) in the FSI results shown in Fig. 10(a) are a little greater than that of classical water-hammer. This effect is counterbalanced by the effect of junction coupling in Fig. 10(b). As it is already known from the literature and can be seen again in Fig. 10, FSI produces greater pressure heads than those of classical water-hammer. Poisson coupling is the distributed interaction of the pressure and the axial stress (strain) waves taking place via the hoop deformation of the pipe wall (Eqs. (13) and (16)). When axial valve movement is allowed, the valve displacements and corresponding stress waves in the pipe wall will strongly interact with the pressure waves in the fluid as a result of local junction coupling (Eqs. (20) and (21)). The analysis with both Poisson and junction coupling (Fig. 10(b)) gives a slightly higher pressure rise in the first half water-hammer cycle compared to the results obtained with only Poisson coupling (Fig. 10(a)).

4.2.3. Simultaneous FSI and viscoelasticity

Figs. 11 and 12 show the combined effects of FSI and viscoelasticity. Computed heads at the valve are shown in Fig. 11, for only Poisson coupling (Fig. 11(a)) and for Poisson and junction coupling (Fig. 11(b)). Fig. 12 depicts computed heads at the locations 5 (Fig. 12(a)) and 8 (Fig. 12(b)) obtained with Poisson and junction coupling. Broken black lines are the results of the full MOC solution, which are deliberately shifted to the right, and continuous blue lines are those of the MOC-FEM solution. Dashed red lines are for the viscoelastic pipe without FSI (Poisson's ratio and valve displacement are both zero).

It is evident that viscoelasticity introduces much damping in the water-hammer results, but FSI still brings about Joukowsky-exceeding pressures in the early moments of the transient event. Slowing down the oscillation, the other important effect of viscoelasticity, is also observed here (compare Figs. 10 and 11) and it is more significant because

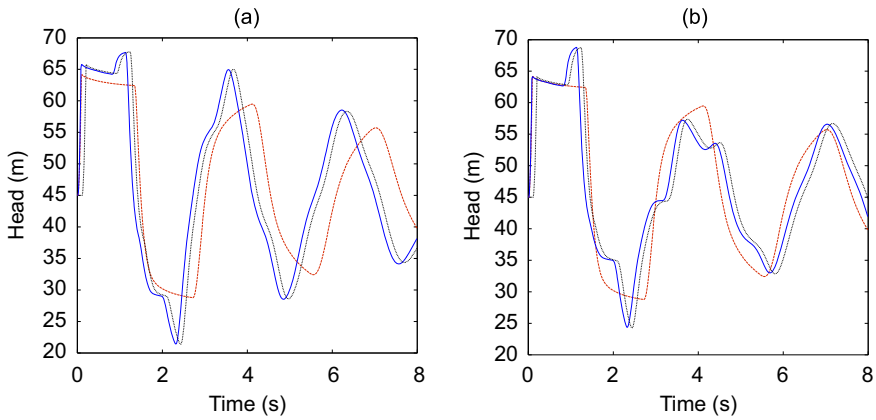

Fig. 11. Pressure head at the valve for the viscoelastic model. (a) With only Poisson coupling, and (b) with Poisson and junction coupling. MOC–FEM solution in continuous blue lines and full MOC solution (with $t=0.1$ s intentional shift) in broken lines; dashed red lines correspond to classical viscoelastic water-hammer. (For interpretation of the references to color in this figure legend, the reader is referred to the web version of this article.)

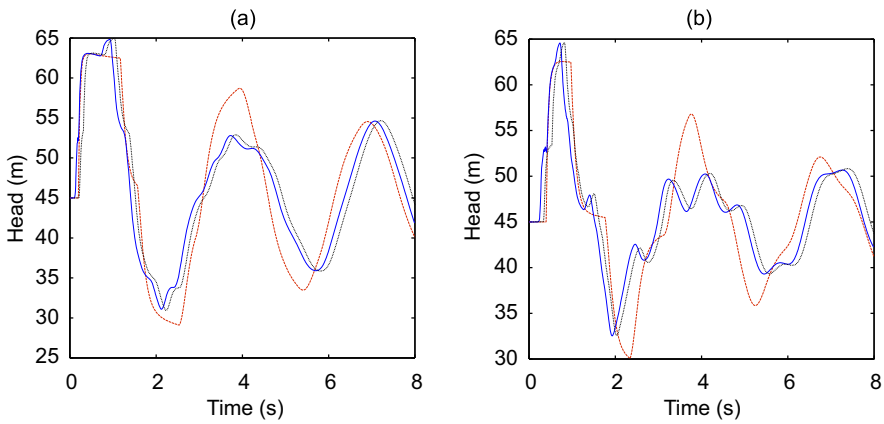

Fig. 12. Pressure head for the viscoelastic model with Poisson and junction coupling. (a) At location 5 and (b) at location 8. MOC–FEM solution in continuous blue lines and full MOC solution (with $t=0.1$ s intentional shift) in broken lines; dashed red lines correspond to classical viscoelastic water-hammer. (For interpretation of the references to color in this figure legend, the reader is referred to the web version of this article.)

junction coupling has such an effect too (compare Fig. 10(a) and (b)). Whilst the leading spring E_0 in the Kelvin–Voigt model fully accounts for the Joukowsky pressure rise, the inclusion of five additional springs E_1–E_5 (Fig. 1), compared to only E_0 in classical viscoelastic water-hammer ($N_{KV}=0$), makes the pipe softer and results in a slower first mode of vibration. Viscoelasticity definitely smoothes the water-hammer transients caused by FSI by progressively eliminating higher frequencies of vibration (Achouyab and Bahrar, 2011; Rachid and Stuckenbruck, 1989).

The importance of viscoelasticity should be assessed from a comparison of the leading retardation times τ_k with the fundamental water-hammer and "solid-hammer" timescales ($4L/c_f$) and ($4L/c_t$). The respective values of 0.05–10 s, 3.0 s and 1.8 s indicate that all effects are of significance here, thereby noting that small effects will be visible in the long term.

5. Conclusion and discussion

A theoretical analysis and numerical simulation of simultaneous FSI and viscoelasticity in an axially movable straight pipeline has been performed. Hydraulic equations were solved using MOC and for this case, comparison of the results with those of experiments carried out at Deltares, Delft, and Imperial College, London, was given as validating evidence. Structural equations were solved using the two numerical methods MOC and FEM. To verify the proposed mathematical model and its numerical implementation, the axial vibration of a viscoelastic bar was simulated and checked against a semi-analytical solution. For FSI in elastic pipes, the results were verified against exact results. For the combined viscoelastic-FSI model, two different numerical approaches were used and their results were compared to show their proper implementation. All comparisons between the results of the current work and the available experimental or (quasi) exact results were satisfactory and so were those between the two different solution methods.

This research is as an extension of previous work on water hammer in viscoelastic pipes, where it was necessary for the whole pipe system to be completely restrained from any kind of axial movement, which can be hard-to-do in practice and error-producing in simulations. The proposed model allows for performing creep-function calibration even when the pipeline has the possibility to move, so it can be used to refine the empirical procedure to obtain the coefficients associated with the Kelvin–Voigt elements. The calibration is mainly based on matching the amount of damping in simulation and experiment, and therefore depends on the quality of both. In water-hammer experiments, damping may come from (unsteady) friction, (unsteady) valve resistance, small amounts of air, wall viscoelasticity, fluid–structure interaction, rubbing, ratcheting and other non-elastic behaviour of supports, radiation to surrounding soil and water, pipe lining, etc. Much of this is unknown and when not (properly) included in the transient solver, the Kelvin–Voigt model will not only represent viscoelasticity, but all the rest too. One remedy, or additional requirement, could be to focus the matching on a typical feature of viscoelasticity, such as the retarding behaviour visible in the zoomed-in detail of Fig. 9 top-right. The FSI part of the transient solver usually suffers from the lack of knowledge of the stiffness and inertia of supports. Also, calibration of a time-dependent viscoelastic Poisson's ratio may be needed here.

Robust and stable results were obtained with both numerical methods (full MOC and MOC–FEM) noting that the viscoelasticity terms were approximated by recursive linear functions of the unknowns at the current time step. The full MOC procedure was the fastest and most accurate method. The MOC–FEM procedure is slower, because of the fluid–structure iterations. It has however the benefit of being more versatile and closer to existing knowledge and software on fluid and structural dynamics; and it is easier to extend if further complications (e.g., plastic wall behaviour, pipe bending, two-phase flow) are to be included.

The investigation of water hammer with FSI and viscoelasticity concerns pipes made of plastic, where FSI effects are more significant than in steel pipes, simply because they are more flexible (although with thicker walls, their modulus of elasticity is lower and their Poisson's ratio is higher). This makes FSI analysis necessary to reliably estimate the ultimate pipe stresses, elbow displacements and anchor forces, especially for designs with flexibly supported pipes. It was found herein that in the early moments of the transient event FSI is significant. Later on viscoelasticity becomes dominant and damps out the oscillations induced by FSI.

Acknowledgements

This study was performed during a one-year sabbatical leave of the first author as visiting Ph.D. student at Eindhoven University of Technology in the Centre for Analysis, Scientific computing and Applications (CASA). He was financially supported by the Iranian Ministry of Science, Research and Technology. The third author is grateful to the China Scholarship Council (CSC) for financially supporting his Ph.D. studies. Thanks are also due to Deltares, Delft, The Netherlands, for making available the water-hammer experimental data obtained in EC-HYDRALAB III Project 022441 (H4976-VFP398).

Appendix A. Derivation of a three-parameter Kelvin–Voigt solid mechanical model

The basic relations which are valid for a three-parameter Kelvin–Voigt solid as depicted in Fig. 1(b) are

$$\sigma = \sigma_0 = \sigma_1, \tag{A.1}$$

$$\varepsilon = \varepsilon_0 + \varepsilon_1, \tag{A.2}$$

where the 0-subscript stands for the sole spring, the 1-subscript corresponds to the two-parameter Kelvin–Voigt element consisting of a dashpot and a spring in parallel, and no-subscript is the characteristic of the whole three-parameter system. The stress–strain relations for σ_0 and σ_1 are

$$\sigma_0 = E_0\varepsilon_0, \tag{A.3}$$

$$\sigma_1 = E_1\varepsilon_1 + \mu_1\dot{\varepsilon}_1. \tag{A.4}$$

The differential constitutive relation between the stress σ and the strain ε is derived as follows. Using (A.1) and (A.3), ε_0 in Eq. (A.2) is replaced by σ/E_0. Then (A.2) is multiplied by E_1 and, separately, it is differentiated with respect to time and multiplied by μ_1. The sum of the two resulting relations is

$$E_1\varepsilon + \mu_1\dot{\varepsilon} = \frac{E_1}{E_0}\sigma + \frac{\mu_1}{E_0}\dot{\sigma} + E_1\varepsilon_1 + \mu_1\dot{\varepsilon}_1. \tag{A.5}$$

With the application of the Eqs. (A.1) and (A.4), this can be written as

$$p_0\sigma + p_1\dot{\sigma} = q_0\varepsilon + q_1\dot{\varepsilon} \quad \text{with} \quad p_0 = 1, \quad p_1 = \frac{\mu_1}{E_0+E_1}, \quad q_0 = \frac{E_0E_1}{E_0+E_1}, \quad q_1 = \frac{E_0\mu_1}{E_0+E_1}. \tag{A.6}$$

This is equivalent to Eq. (2) for $N_{\mathrm{KV}}=1$. The initial condition for a three-parameter Kelvin–Voigt solid is taken as (Wineman and Rajagopal, 2000)

$$p_1\sigma(0) = q_1\varepsilon(0). \tag{A.7}$$

A proper statement of the constitutive equation describing the three-parameter solid consists of the differential relation (A.6) together with the initial condition (A.7).

To arrive at the integral representation of the constitutive equation, the Laplace operator is used:

$$L(f(t)) = \bar{f}(s) := \int_0^\infty f(t)e^{-st}dt. \tag{A.8}$$

Using integration by parts, the Laplace transform of the derivative of a function is

$$L\left(\frac{df}{dt}(t)\right) = sL(f(t)) - f(0) = s\bar{f}(s) - f(0). \tag{A.9}$$

The convolution integral $f_3(t)$ of two functions $f_1(t)$ and $f_2(t)$ is denoted by $f_3(t)=f_1(t)*f_2(t)$ and defined as

$$f_3(t) := \int_0^t f_1(t-s)f_2(s)ds. \tag{A.10}$$

Then, this important property holds:

$$L(f_3(t)) = \bar{f}_3(s) = L(f_1(t)*f_2(t)) = L(f_1(t))L(f_2(t)) = \bar{f}_1(s)\bar{f}_2(s). \tag{A.11}$$

Taking the Laplace transform of Eq. (A.6) yields

$$p_0\bar{\sigma} + p_1(s\bar{\sigma} - \sigma(0)) = q_0\bar{\varepsilon} + q_1(s\bar{\varepsilon} - \varepsilon(0)). \tag{A.12}$$

Substituting the initial condition (A.7) gives

$$\bar{\varepsilon}(s) = \left(\frac{p_0 + p_1 s}{q_0 + q_1 s}\right)\bar{\sigma}(s). \tag{A.13}$$

By introducing $\tau_1 := \mu_1/E_1$, $J_1 := 1/E_1$ and $J_0 := 1/E_0$ in Eq. (A.6), Eq. (A.13) becomes

$$\bar{\varepsilon}(s) = \bar{\sigma}(s)s\left(\frac{J_0+J_1}{s} - \frac{J_1\tau_1}{s\tau_1+1}\right) := \bar{\sigma}(s)s\bar{J}(s), \quad \text{where} \quad \bar{J}(s) := \left(\frac{J_0+J_1}{s} - \frac{J_1\tau_1}{s\tau_1+1}\right). \tag{A.14}$$

If this is written as

$$\bar{\varepsilon}(s) = \bar{\sigma}(s)(s\bar{J}(s) - J(0)) + \bar{\sigma}(s)J(0), \tag{A.15}$$

then, according to Eq. (A.9), it becomes

$$\bar{\varepsilon}(s) = \bar{\sigma}(s)L\left(\frac{dJ}{dt}(t)\right) + \bar{\sigma}(s)J(0), \quad \text{where} \quad J(t) = J_0 + J_1(1 - e^{-(t/\tau_1)}), \tag{A.16}$$

and, using property (A.11), it reads

$$\bar{\varepsilon}(s) = L\left(\sigma(t)*\frac{dJ}{dt}(t)\right) + \bar{\sigma}(s)J(0), \tag{A.17}$$

which is the Laplace transform of

$$\varepsilon(t) = \sigma(t)J(0) + \int_0^t \sigma(t-s)\frac{dJ}{ds}(s)ds. \tag{A.18}$$

It is convenient to introduce the simplifying Stieltjes notation for the convolution of two functions $G(t)$ and $Q(t)$ (they are equal to zero for $t<0$ and piecewise continuous for $t\geq 0$) as follows (Wineman and Rajagopal, 2000):

$$(G*dQ)(t) := G(t)Q(0)+\int_0^t G(t-s)\frac{dQ}{ds}(s)ds. \tag{A.19}$$

Now, Eq. (A.18) can simply be denoted as

$$\varepsilon(t)=\sigma*dJ(t). \tag{A.20}$$

Appendix B. Derivation of Eq. (13)

Starting from the following forms of the continuity equation for the fluid, taking into account the constitutive circumferential strain–stress relation for viscoelastic materials, knowing that for thin-walled pipes Eq. (10) holds, ignoring σ_r with respect to σ_ϕ, and assuming that Poisson's ratio is constant:

$$\frac{\partial V}{\partial z}+\frac{\rho_f g}{K}\frac{\partial H}{\partial t}+2\frac{\partial \varepsilon_\phi}{\partial t}=0 \quad \text{with} \quad \varepsilon_\phi=\sigma_\phi*dJ-\upsilon(\sigma_z*dJ), \quad \text{or}$$

$$\frac{\partial V}{\partial z}+\frac{\rho_f g}{K}\frac{\partial H}{\partial t}+2\frac{\partial(\sigma_\phi*dJ)}{\partial t}-2\upsilon\frac{\partial(\sigma_z*dJ)}{\partial t}=0 \quad \text{with} \quad \sigma_\phi=\rho_f g\frac{\tilde{H}D}{2e}, \tag{B.1}$$

$$\frac{\partial V}{\partial z}+\frac{\rho_f g}{K}\frac{\partial H}{\partial t}+\rho_f g\frac{D}{e}\frac{\partial(\tilde{H}*dJ)}{\partial t}-2\upsilon\frac{\partial(\sigma_z*dJ)}{\partial t}=0. \tag{B.2}$$

To deal with the last term of Eq. (B.2), the time derivative is taken of Eq. (11), and using Eq. (10) and $\varepsilon_z=\partial u_z/\partial z$, one can write

$$\frac{\partial(\sigma_z*dJ)}{\partial t}=\frac{\partial \dot{u}_z}{\partial z}+\frac{\upsilon D}{2e}\rho_f g\frac{\partial(\tilde{H}*dJ)}{\partial t}. \tag{B.3}$$

Substituting (B.3) in (B.2), the continuity equation becomes

$$\frac{\partial V}{\partial z}+\frac{\rho_f g}{K}\frac{\partial H}{\partial t}-2\upsilon\frac{\partial \dot{u}_z}{\partial z}+(1-\upsilon^2)\rho_f g\frac{D}{e}\frac{\partial(\tilde{H}*dJ)}{\partial t}=0. \tag{B.4}$$

With the definition of the Stieltjes convolution operator (A.19) and noting that $\partial\tilde{H}/\partial t=\partial H/\partial t$, this is written as

$$\frac{\partial V}{\partial z}+\frac{\rho_f g}{K}\frac{\partial H}{\partial t}-2\upsilon\frac{\partial \dot{u}_z}{\partial z}+(1-\upsilon^2)\rho_f g\frac{D}{e}\left(\frac{\partial H}{\partial t}J(0)+\frac{\partial}{\partial t}\left(\int_0^t \tilde{H}(t-s)\frac{dJ}{ds}(s)ds\right)\right)=0. \tag{B.5}$$

Using $J(0)=J_0=1/E_0$ and definition (5), Eq. (13) is obtained.

Appendix C. Derivation of Eq. (19)

Taking the derivative of Eq. (11) with respect to z and using $\varepsilon_z=\partial u_z/\partial z$ one can write

$$\frac{\partial^2 u_z}{\partial z^2}=\frac{\partial \sigma_z}{\partial z}*dJ-\upsilon\frac{\partial(\sigma_\phi*dJ)}{\partial z}. \tag{C.1}$$

The Leibniz rule for differentiation of integrals was used in deriving the first term on the right, which is valid if σ_z and its z-derivative are piecewise continuous. Substituting $\partial\sigma_z/\partial z$ from Eq. (18) leads to

$$\frac{\partial^2 u_z}{\partial z^2}=\left(\rho_t\frac{\partial \dot{u}_z}{\partial t}*dJ\right)-\upsilon\frac{\partial(\sigma_\phi*dJ)}{\partial z}. \tag{C.2}$$

With Eq. (10) this reduces to

$$\frac{\partial^2 u_z}{\partial z^2}=\rho_t\left(\frac{\partial \dot{u}_z}{\partial t}*dJ\right)-\rho_f g\frac{\upsilon D}{2e}\frac{\partial(\tilde{H}*dJ)}{\partial z}. \tag{C.3}$$

Writing out the Stieltjes convolution operator (A.19) gives

$$\frac{\partial^2 u_z}{\partial z^2}=\rho_t\left(\ddot{u}_z J(0)+\int_0^t \ddot{u}_z(t-s)\frac{dJ}{ds}(s)ds\right)-\rho_f g\frac{\upsilon D}{2e}\left(\frac{\partial\tilde{H}}{\partial z}J(0)+\frac{\partial}{\partial z}\left(\int_0^t \tilde{H}(t-s)\frac{dJ}{ds}(s)ds\right)\right). \tag{C.4}$$

After multiplication by $c_t^2=E_0/\rho_t$ and replacement of the integrals by the definitions (5) and (7), Eq. (19) is obtained.

Appendix D. A numerical approximation of the convolution integral

The applied numerical approximation of the convolution integral appearing in many of the equations is obtained as follows:

$$
\begin{aligned}
I_k(t) &= \frac{J_k}{\tau_k}\int_0^t h(t-s)\mathrm{e}^{-s/\tau_k}ds = \underbrace{\frac{J_k}{\tau_k}\int_0^{\Delta t} h(t-s)\mathrm{e}^{-s/\tau_k}ds}_{\mathrm{A}} + \underbrace{\frac{J_k}{\tau_k}\int_{\Delta t}^{t} h(t-s)\mathrm{e}^{-s/\tau_k}ds}_{\mathrm{B}} \\
\mathrm{A} &= \frac{J_k}{\tau_k}\int_0^{\Delta t} h(t-s)\mathrm{e}^{-s/\tau_k}ds = -\frac{J_k}{\tau_k}\int_t^{t-\Delta t} h(y)\mathrm{e}^{(y-t)/\tau_k}dy = \frac{J_k}{\tau_k}\mathrm{e}^{-t/\tau_k}\int_{t-\Delta t}^{t} h(y)\mathrm{e}^{y/\tau_k}dy \\
&= \frac{J_k}{\tau_k}\mathrm{e}^{-t/\tau_k}\left(h(y)\tau_k\mathrm{e}^{y/\tau_k}\Big|_{t-\Delta t}^{t} - \int_{t-\Delta t}^{t}\frac{\partial h}{\partial y}(y)\tau_k\mathrm{e}^{y/\tau_k}dy\right) = \frac{J_k}{\tau_k}\mathrm{e}^{-t/\tau_k}\left(h(t)\tau_k\mathrm{e}^{t/\tau_k} - h(t-\Delta t)\tau_k\mathrm{e}^{(t-\Delta t)/\tau_k} - \int_{t-\Delta t}^{t}\frac{\partial h}{\partial y}(y)\tau_k\mathrm{e}^{y/\tau_k}dy\right) \\
&\approx \frac{J_k}{\tau_k}\mathrm{e}^{-t/\tau_k}\left(h(t)\tau_k\mathrm{e}^{t/\tau_k} - h(t-\Delta t)\tau_k\mathrm{e}^{(t-\Delta t)/\tau_k} - \tau_k\dot{h}(t-\Delta t)\int_{t-\Delta t}^{t}\mathrm{e}^{y/\tau_k}dy\right) \\
&\approx \frac{J_k}{\tau_k}\mathrm{e}^{-t/\tau_k}(h(t)\tau_k\mathrm{e}^{t/\tau_k} - h(t-\Delta t)\tau_k\mathrm{e}^{(t-\Delta t)/\tau_k} - \tau_k\dot{h}(t-\Delta t)[\tau_k\mathrm{e}^{y/\tau_k}]_{t-\Delta t}^{t}) \\
&\approx \frac{J_k}{\tau_k}\mathrm{e}^{-t/\tau_k}\left(h(t)\tau_k\mathrm{e}^{t/\tau_k} - h(t-\Delta t)\tau_k\mathrm{e}^{(t-\Delta t)/\tau_k} - \tau_k^2\left(\frac{h(t)-h(t-\Delta t)}{\Delta t}\right)(\mathrm{e}^{t/\tau_k} - \mathrm{e}^{(t-\Delta t)/\tau_k})\right) \\
&\approx J_k h(t) - J_k h(t-\Delta t)\mathrm{e}^{-\Delta t/\tau_k} - J_k\tau_k\left(\frac{h(t)-h(t-\Delta t)}{\Delta t}\right)(1-\mathrm{e}^{-\Delta t/\tau_k}) \\
&\approx h(t)\left(J_k - \frac{J_k\tau_k}{\Delta t}\left(1-\mathrm{e}^{-\Delta t/\tau_k}\right)\right) + h(t-\Delta t)\left(-J_k\mathrm{e}^{-\Delta t/\tau_k} + \frac{J_k\tau_k}{\Delta t}(1-\mathrm{e}^{-\Delta t/\tau_k})\right) \\
\mathrm{B} &= \int_{\Delta t}^{t} h(t-s)\frac{J_k}{\tau_k}\mathrm{e}^{-s/\tau_k}ds = \int_0^{t-\Delta t} h(t-\Delta t-u)\frac{J_k}{\tau_k}\mathrm{e}^{(-u-\Delta t)/\tau_k}du = \mathrm{e}^{-\Delta t/\tau_k}\int_0^{t-\Delta t} h(t-\Delta t-u)\frac{J_k}{\tau_k}\mathrm{e}^{-u/\tau_k}du = \mathrm{e}^{-\Delta t/\tau_k}I_k(t-\Delta t)
\end{aligned}
\tag{D.1}
$$

Appendix E. Diagonalization of Eq. (37)

Considering Eq. (37), from $|\mathbf{B}-\lambda\mathbf{A}| = 0$, the eigenvalues λ_i are obtained as

$$\hat{c}_f = \lambda_1 = -\lambda_2 = \sqrt{\frac{1}{2}\left\{\gamma^2 - \sqrt{\gamma^4 - 4c_f^2c_t^2}\right\}}, \quad \gamma = c_f^2 + c_t^2 + 2v^2\frac{\rho_f}{\rho_t}\frac{R}{e}c_f^2, \tag{E.1}$$

$$\hat{c}_t = \lambda_3 = -\lambda_4 = \sqrt{\frac{1}{2}\left\{\gamma^2 + \sqrt{\gamma^4 - 4c_f^2c_t^2}\right\}}. \tag{E.2}$$

To decouple the system of Eq. (37) into four independent ordinary differential equations, it is multiplied by $\mathbf{T}$ where $\mathbf{T}=\mathbf{S}^{-1}\mathbf{A}^{-1}$ and $\mathbf{S}$ is the matrix of eigenvectors corresponding to the eigenvalues λ_i. As a result, the diagonal matrix of eigenvalues $\mathbf{\Lambda}$ satisfies the relation

$$\mathbf{S}^{-1}(\mathbf{A}^{-1}\mathbf{B})\mathbf{S} = \mathbf{\Lambda}. \tag{E.3}$$

Right multiplication by $\mathbf{S}^{-1}$ and using $\mathbf{S}^{-1}=\mathbf{TA}$ results in

$$\mathbf{TB} = \mathbf{\Lambda TA}, \tag{E.4}$$

so that with $\mathbf{v}=\mathbf{TAy}$ Eq. (37) can be rewritten as

$$\frac{\partial\mathbf{v}}{\partial t} + \mathbf{\Lambda}\frac{\partial\mathbf{v}}{\partial z} = \mathbf{Tr} \quad \text{or} \quad \frac{\partial v_i}{\partial t} + \lambda_i\frac{\partial v_i}{\partial z} = (\mathbf{Tr})_i, \quad i = 1,2,3,4. \tag{E.5}$$

The characteristic paths in the distance-time plane satisfy $\lambda_i = dz/dt$ so that along these lines

$$\frac{dv_i}{dt} = (\mathbf{Tr})_i. \tag{E.6}$$

The above relation is integrated numerically. With $\mathbf{v} = \mathbf{S}^{-1}\mathbf{y} = \mathbf{TAy}$ the compatibility Eqs. (E.6) are written in terms of the original unknowns $\mathbf{y}$. Writing the terms v_i and $(\mathbf{Tr})_i$ in their expanded form, Eq. (E.6) becomes

$$(\mathbf{TA})_{i1}\frac{dy_1}{dt} + (\mathbf{TA})_{i2}\frac{dy_2}{dt} + (\mathbf{TA})_{i3}\frac{dy_3}{dt} + (\mathbf{TA})_{i4}\frac{dy_4}{dt} = T_{i1}r_1 + T_{i2}r_2 + T_{i3}r_3 + T_{i4}r_4. \tag{E.7}$$

Appendix F. The correspondence principle

If the Laplace transform is taken of Eq. (3), using property (A.11) and then (A.9), one obtains

$$\bar{\varepsilon}(s) = \bar{\sigma}(s)J(0) + \bar{\sigma}(s)L\left(\frac{dJ}{dt}(t)\right) = \bar{\sigma}(s)J(0) + \bar{\sigma}(s)(s\bar{J}(s) - J(0)) = s\bar{J}(s)\bar{\sigma}(s) := \bar{J}^*(s)\bar{\sigma}(s), \tag{F.1}$$

where $\bar{J}^*(s)$ is s times the Laplace transform of the time-dependent creep function $J(t)$. The equation can be thought of as Hooke's law for a linear viscoelastic material and it is sometimes referred to as Alfrey's correspondence principle. This leads to a general method to solve many practical viscoelastic boundary value problems in a simple manner: the solution can be obtained in the Laplace domain (transformation with respect to time) by simply replacing the constant inverse of the elastic modulus $1/E = J_0$ in the corresponding Laplace transformed elastic problem by $\bar{J}^*(s) = s\bar{J}(s)$. Then by taking the inverse Laplace transform (numerically), the solution is found in the time domain.

Appendix G. Exact solution of axial vibration of an elastic bar subjected to a step force

An analytical solution of the problem described by the Eqs. (47)–(49a, b) can be obtained by adding together the solutions of two similar problems defined by the PDE (47), but each with changed initial and boundary conditions

$$u_z(z,0) = \frac{F_0 z}{E_0 A_t}, \quad \frac{\partial u_z}{\partial t}(z,0) = 0, \quad u_z(0,t) = 0, \quad \frac{\partial u_z}{\partial z}(L,t) = \frac{F_0}{E_0 A_t}, \tag{G.1}$$

$$u_z(z,0) = -\frac{F_0 z}{E_0 A_t}, \quad \frac{\partial u_z}{\partial t}(z,0) = 0, \quad u_z(0,t) = 0, \quad \frac{\partial u_z}{\partial z}(L,t) = 0. \tag{G.2}$$

The first problem, described by the Eqs. (47) and (G.1), starts from equilibrium and is equivalent to the static problem governed by $(\partial^2 u_z/\partial z^2) = 0$ with the bar subjected to a constant force F_0 at one end. There is no excitation and the trivial solution of the problem is

$$u_z(z,t) = \frac{F_0 z}{E_0 A_t}. \tag{G.3}$$

The linear function given by (G.3) is expressed by the Fourier sine series

$$u_z(z,t) = \frac{8}{\pi^2}\frac{F_0 L}{A_t E_0} \sum_{n=1,3,\ldots}^{\infty} \frac{(-1)^{(n-1)/2}}{n^2} \sin\frac{n\pi z}{2L}. \tag{G.4}$$

The second problem, described by the Eqs. (47) and (G.2), has homogeneous boundary conditions and a non-equilibrium initial condition. It can be solved by separation of variables, yielding

$$u_z(z,t) = \frac{8}{\pi^2}\frac{F_0 L}{A_t E_0} \sum_{n=1,3,\ldots}^{\infty} \frac{(-1)^{(n+1)/2}}{n^2} \sin\frac{n\pi z}{2L} \cos\frac{n\pi t c_t}{2L}. \tag{G.5}$$

Summing the expressions (G.4) (or (G.3)) and (G.5) gives the desired solution of the problem, that is Eq. (50).

If one wishes to check if this solution (Eq. (50)) satisfies the boundary conditions (49a, b), one should be aware that the Fourier sine series (like (G.4)) of a function cannot in general be differentiated term by term. This matter and the theorem to properly differentiate them are discussed in detail by Haberman (2004).

References

Achouyab, E.H., Bahrar, B., 2011. Numerical modeling of phenomena of waterhammer using a model of fluid–structure interaction. Comptes Rendus Mécanique 339, 262–269.

Ahmadi, A., Keramat, A., 2010. Investigation of fluid–structure interaction with various types of junction coupling. Journal of Fluids and Structures 26, 1123–1141.

Bahrar, B., Rieutord, E., Morel, R., 1998. Influence de la viscoélasticité de la paroi sur les phénomènes classiques de coup de bélier. La Houille Blanche, 26–32 (in French).

Bergant, A., Hou, Q., Keramat, A., Tijsseling, A.S., 2011. Experimental and numerical analysis of water hammer in a large-scale PVC pipeline apparatus, in: Proceedings of the Fourth IAHR International Meeting on Cavitation and Dynamic Problems in Hydraulic Machinery and Systems, Belgrade, Serbia, October 2011, pp. 27–36.

Bergant, A., Tijsseling, A., Vítkovský, J.P., Covas, D., Simpson, A., Lambert, M., 2008a. Parameters affecting water–hammer wave attenuation, shape and timing. Part 1: Mathematical tools. IAHR Journal of Hydraulic Research 46, 373–381.

Bergant, A., Tijsseling, A., Vítkovský, J.P., Covas, D., Simpson, A., Lambert, M., 2008b. Parameters affecting water–hammer wave attenuation, shape and timing. Part 2: Case studies. IAHR Journal of Hydraulic Research 46, 382–391.

Bergant, A., van't Westende, J.M.C., Koppel, T., Gale, J., Hou, Q., Pandula, Z., Tijsseling, A.S., 2010. Water hammer and column separation due to accidental simultaneous closure of control valves in a large scale two-phase flow experimental test rig, in: Proceedings of the ASME Pressure Vessels and Piping Division Conference, Bellevue, USA, July 2010, Paper PVP2010-26131.

Brinson, H.F., Brinson, L.C., 2008. Polymer Engineering Science and Viscoelasticity—An Introduction. Springer.

Bughazem, M.B., Anderson, A., 2000. Investigation of an unsteady friction model for waterhammer and column separation, in: Proceedings of the Eighth International Conference on Pressure Surges, The Hague, The Netherlands, pp. 483–498.

Covas, D., Stoianov, I., Mano, J., Ramos, H., Graham, N., Maksimovic, C., 2004a. The dynamic effect of pipe-wall viscoelasticity on hydraulic transients, Part I—experimental analysis and creep characterization. IAHR Journal of Hydraulic Research 42, 516–530.

Covas, D., Stoianov, I., Mano, J., Ramos, H., Graham, N., Maksimovic, C., 2005. The dynamic effect of pipe-wall viscoelasticity in hydraulic transients, Part II—model development, calibration and verification. IAHR Journal of Hydraulic Research 43, 56–70.

Covas, D., Stoianov, I., Ramos, H., Graham, N., Maksimovic, C., Butler, D., 2004b. Water hammer in pressurized polyethylene pipes: conceptual model and experimental analysis. Urban Water Journal 1, 177–197.

Duan, H.F., Ghidaoui, M., Lee, P.J., Tung, Y.K., 2010. Unsteady friction and visco-elasticity in pipe fluid transients. IAHR Journal of Hydraulic Research 48, 354–362 (Discussion in 49, 398–403).

Elansary, A.S., Silva, W., Chaudhry, M.H., 1994. Numerical and experimental investigation of transient pipe flow. IAHR Journal of Hydraulic Research 32, 689–706.

Fan, D., Tijsseling, A., 1992. Fluid–structure interaction with cavitation in transient pipe flows. ASME Journal of Fluids Engineering 114, 268–274.
Haberman, H., 2004. Applied Partial Differential Equations with Fourier Series and Boundary Value Problems, 4th edition. Prentice Hall, pp. 116–124.
Hachem, F.E., Schleiss, A.J., 2011. A review of wave celerity in frictionless and axisymmetrical steel-lined pressure tunnels. Journal of Fluids and Structures 27, 311–328.
Hadj-Taïeb, L., Hadj-Taïeb, E., 2009. Numerical simulation of transient flows in viscoelastic pipes with vapour cavitation. International Journal of Modelling and Simulation 29, 206–213.
Hambric, S.A., Boger, D.A., Fahnline, J.B., Campbell, R.L., 2010. Structure- and fluid-borne acoustic power sources induced by turbulent flow in 90° piping elbows. Journal of Fluids and Structures 26, 121–147.
Heinsbroek, A.G.T.J., 1997. Fluid–structure interaction in non-rigid pipeline systems. Nuclear Engineering and Design 172, 123–135.
Heinsbroek, A.G.T.J., Tijsseling, A.S., 1994. The influence of support rigidity on waterhammer pressures and pipe stresses, in: Proceedings of the Second International Conference on Water Pipeline Systems, BHR Group, Edinburgh, UK, pp. 17–30.
Hoog, F.R., de, Knight, J.H., Stokes, A.N., 1982. An improved method for numerical inversion of Laplace transforms. SIAM Journal of Scientific and Statistical Computing 3, 357–366.
Keramat, A., Tijsseling, A.S., Ahmadi, A., 2010. Investigation of transient cavitating flow in viscoelastic pipes. IOP Conference Series: Earth and Environmental Science 12 (1), 012081.
Laanearu, J., Bergant, A., Annus, I., Koppel, T., van't Westende, J.M.C., 2009. Some aspects of fluid elasticity related to filling and emptying of large-scale pipeline, in: Proceedings of the Third IAHR International Meeting of the Workgroup on Cavitation and Dynamic Problems in Hydraulic Machinery and Systems, Brno, Czech Republic, October 2009, pp. 465–474.
Lavooij, C.S.W., Tijsseling, A.S., 1991. Fluid–structure interaction in liquid-filled piping systems. Journal of Fluids and Structures 5, 573–595.
Li, Q.S., Ke, Yang, Zhang, L., 2003. Analytical solution for fluid–structure interaction in liquid-filled pipes subjected to impact-induced water hammer. ASCE Journal of Engineering Mechanics 129, 1408–1417.
Narayanan, G.V., Beskos, D.E., 1982. Numerical operational methods for time-dependent linear problems. International Journal for Numerical Methods in Engineering 18, 1829–1854.
Neuhaus, T., Dudlik, A., 2006. Experiments and comparing calculations on thermohydraulic pressure surges in pipes. Kerntechnik 71, 87–94.
Papargyri-Beskou, S., Beskos, D.E., 2004. Response of gradient-viscoelastic bar to static and dynamic axial load. Acta Mechanica 170, 199–212.
Prek, M., 2004. Wavelet analysis of sound signal in fluid-filled viscoelastic pipes. Journal of Fluids and Structures 19, 63–72.
Prek, M., 2007. Analysis of wave propagation in fluid-filled viscoelastic pipes. Mechanical Systems and Signal Processing 21, 1907–1916.
Rachid, F.B.F., Costa Mattos, H.S., 1995. Pressure transients in damageable elasto-plastic pipes, in: Proceedings of the Joint ASME/JSME Pressure Vessel and Piping Conference, Honolulu, USA, ASME-PVP 301, pp. 31–40.
Rachid, F.B.F., Costa Mattos, H.S., 1998a. Modelling of pipeline integrity taking into account the fluid–structure interaction. International Journal for Numerical Methods in Fluids 28, 337–355.
Rachid, F.B.F., Costa Mattos, H.S., 1998b. Modelling the damage induced by pressure transients in elasto-plastic pipes. Meccanica 33, 139–160.
Rachid, F.B.F., da Gama, R.M.S., Costa Mattos, H.S., 1994. Modelling of hydraulic transients in damageable elasto-viscoplastic piping systems. Applied Mathematical Modelling 18, 207–215.
Rachid, F.B.F., Stuckenbruck, S., 1989. Transients in liquid and structure in viscoelastic pipes, in: Proceedings of the Sixth International Conference on Pressure Surges, Cambridge, UK, pp. 69–84.
Soares, A.K., Covas, D.I.C., Ramos, H.M., Reis, L.F.R., 2009. Unsteady flow with cavitation in viscoelastic pipes. International Journal of Fluid Machinery and Systems 2, 269–277.
Soares, A.K., Covas, D.I.C., Reis, L.F.R., 2008. Analysis of PVC pipe-wall viscoelasticity during water hammer. ASCE Journal of Hydraulic Engineering 134, 1389–1394.
Tijsseling, A.S., 1996. Fluid–structure interaction in liquid-filled pipe systems: a review. Journal of Fluids and Structures 10, 109–146.
Tijsseling, A.S., 2003. Exact solution of linear hyperbolic four-equation system in axial liquid-pipe vibration. Journal of Fluids and Structures 18, 179–196.
Tijsseling, A.S., 2007. Water hammer with fluid–structure interaction in thick-walled pipes. Computers and Structures 85, 844–851.
Tijsseling, A.S., 2009. Exact computation of the axial vibration of two coupled liquid-filled pipes, in: Proceedings of the ASME Pressure Vessels and Piping Division Conference, Prague, Czech Republic, July 2009, Paper PVP2009-77250.
Tijsseling, A.S., Heinsbroek, A.G.T.J., 1999. The influence of bend motion on waterhammer pressures and pipe stresses, in: Proceedings of the Third ASME & JSME Joint Fluids Engineering Conference, Symposium S-290 Water Hammer, San Francisco, USA, July 1999, ASME-FED 248, Paper FEDSM99-6907.
Tijsseling, A.S., Kruisbrink, A.C.H., Pereira da Silva, A., 1999. The reduction of pressure wavespeeds by internal rectangular tubes, in: Proceedings the of Third ASME & JSME Joint Fluids Engineering Conference, Symposium S-290 Water Hammer, San Francisco, USA, July 1999, ASME-FED 248, Paper FEDSM99-6903.
Tijsseling, A.S., Vardy, A.E., 1996. On the suppression of coupled liquid/pipe vibrations, in: Proceedings of the 18th IAHR Symposium on Hydraulic Machinery and Cavitation, Valencia, Spain, pp. 945–954.
Tijsseling, A.S., Vardy, A.E., 2005. FSI and transient cavitation tests in a T-piece pipe. Journal of Fluids and Structures 20, 753–762.
Tijsseling, A.S., Vardy, A.E., Fan, D., 1996. Fluid–structure interaction and cavitation in a single-elbow pipe system. Journal of Fluids and Structures 10, 395–420.
Warda, H.A., Elashry, Y., 2010. Towards an improved understanding of water-hammer column-separation due to rapid valve closure, in: Proceedings of the ASME Pressure Vessels and Piping Division Conference, Bellevue, USA, July 2010, Paper PVP2010-26146.
Weijde, P.J. van der, 1985. Prediction of pressure surges and dynamic forces in pipeline systems, influence of system vibrations on pressures and dynamic forces (fluid–structure interaction), in: Transactions of the Symposium on Pipelines, Utrecht, The Netherlands, November 1985, The Institution of Chemical Engineers, European Branch Symposium Series 4, pp. 327–335.
Wiggert, D.C., Tijsseling, A.S., 2001. Fluid transients and fluid–structure interaction in flexible liquid-filled piping. ASME Applied Mechanics Reviews 54, 455–481.
Williams, D.J., 1977. Waterhammer in non-rigid pipes: precursor waves and mechanical damping. IMechE Journal of Mechanical Engineering Science 19 (6), 237–242.
Wineman, A.S., Rajagopal, K.R., 2000. Mechanical Response of Polymers—An Introduction. Cambridge University Press.